2D DOSE MEASUREMENT USING A FLAT PANEL EPID

by

Seng Boh Lim

B.A.Sc. (Hons.), University of British Columbia, 1994
M.A.Sc., University of British Colombia, 1996
M.Eng, University of British Columbia, 2002

A THESIS SUBMITTED IN PARTIAL FULFILLMENT
OF THE REQUIREMENTS FOR THE DEGREE OF
MASTER OF SCIENCE
in
THE FACULTY OF GRADUATE STUDIES
(Physics)

THE UNIVERSITY OF BRITISH COLUMBIA
(Vancouver)

August 2008

©Seng Boh Lim, 2008

Abstract

The increasing use of intensity modulated radiation therapy (IMRT) to deliver conformal radiation treatment has prompted the search for a faster and more cost effective quality assurance (QA) system. The standard technique relies on the use of film for two-dimensional dose distribution verification. Although film is considered the gold standard and is widely used for this purpose, the procedures involved are relatively lengthy, labour intensive and costly for a multiple field IMRT verification. In this study, we investigate the use of an amorphous silicon electronic portal imaging device (a-Si EPID) to complement the film. The dosimetric behaviour of the device is studied both experimentally and numerically using the EGSnrc Monte Carlo simulation routine. The intrinsic build-up of the flat panel EPID was found to be 1.1 cm of water equivalent material. The response of the flat panel EPID was found to be linear between 0 and 300 cGy. To calibrate the flat panel EPID for two dimensional dose measurements, the deconvolution method was chosen. The scatter dose kernel required for this calibration method was calculated and characterized by varying the energy, spectrum and phantom material using a 6MV pencil beam. We found that flat panel EPID scatter kernel has as much as 80% more scattering power than the water scatter kernel in the region 1 cm away from the center of a 6MV pencil beam. This confirms that a flat panel EPID behaves significantly differently from water dosimetrically and requires an accurate dose scatter kernel for calibration. A 1.0 cm wide picket fence test pattern was used to test the accuracy of the kernel. Using the deconvolution method with the calculated dose kernels, the measurements from the flat panel EPID show improved agreement with the films.

Table of Contents

Abstract ..... **ii**
Table of Contents ..... **iii**
List of Figures ..... **v**
1. Introduction **1**
1.1. Background 1
1.2. Film Dosimetry 2
1.3. Electronic Portal Imaging Devices 2
1.3.1. Flat Panel EPID 3
1.3.2. Dosimetry 5
1.4. Film and Portal Imaging Workflow Comparison 7
1.5. Motivation 8
2. Method **9**
2.1. Equivalent Build-up Depth 9
2.2. Dose Linearity Response 9
2.3. Scatter Kernel Determination 9
2.3.1. 6MV X-ray Beam Energy Spectrum Simulation 10
2.3.2. Scatter Kernel Simulation 10
2.4. Verification 11
2.4.1. Verification of Monte Carlo Calculation 11
2.4.1.1. Spectrum 12
2.4.1.2. Energy Effect 12
2.4.1.3. Phantom Material 12
2.4.2. Experimental Verification 12
2.4.2.1. Deconvolution Kernel 12
2.4.2.2. Test Pattern 12
2.4.2.3. Comparison 13
3. Results **14**
3.1. Inherent Water Equivalent Build-up Thickness 14
3.2. Dose Linearity Response 14
3.3. Scatter Kernel 15
3.3.1. 6MV X-ray Beam Energy Spectrum 15
3.3.2. Scatter Kernel Simulation 16
3.4. Verification 17
3.4.1. Verification of Monte Carlo Simulation 17
3.4.1.1. Spectrum Effect 17
3.4.1.2. Energy Effect 19
3.4.1.3. Phantom Material 20
3.4.2. Experimental Verification 22
3.4.2.1. Deconvolution Kernel 22
3.4.2.2. Test Pattern 22
3.4.2.3. Profile Comparison 23
4. Discussion **25**
4.1. Inherent Water Equivalent Build-up Thickness 25

4.2. Dose Linearity Response 25
4.3. Scatter Kernel 25
4.3.1. 6MV X-ray Beam Energy Spectrum 25
4.3.2. Scatter Kernel Simulation 25
4.4. Verification 26
4.4.1. Verification of Monte Carlo Simulation 26
4.4.1.1. Spectral Effect 26
4.4.1.2. Phantom Effect 26
4.4.2. Experimental Verification 27
4.4.2.1. Deconvolution Kernel 27
4.4.2.2. Test Pattern 27
4.4.2.3. Profile Comparison 27
5. Conclusions 28
6. References 29
Appendix I. SLIC and Video-Based EPIDs 31
I.A. Scanning Liquid Ionization Chamber (SLIC) 31
I.B. Video-Based EPID 32
Appendix II. Other Dose Calculation Methods 34
II.A. Empirical Method 34
II.B. Two-Step Convolution Algorithm 36
Appendix III. Matlab Codes for Registration 39
III.A. Top Level Program 39
III.B. Program: mydicomread.m 40
III.C. Program: eflread.m 40
III.D. Program: pointcapture.m 41
III.E. Program: swcentroid.m 41
III.F. Program: regMatrix.m 41
III.G. Program: srt_efl1.m 42
Appendix IV. Monte Carlo Simulation Input File 44

List of Figures

Figure 1-1: Two types of radiation detectors are shown here. (a) Indirect detector converts incident radiation into secondary electrons which are converted into visible light for detection; (b) Direct detector converts radiation directly into secondary electron for detection. 3
Figure 1-2: An array of photodiodes used for the flat panel imager is shown. Each photodiode collects visible photons generated by the high energy x-rays. The data are read out through the data line and the timing is controlled by the control FET. The bias line is used to control the bias to the photodiode and the charge-up line is used to control the opening and closing of the control FET. 4
Figure 1-3: Measurement from the flat panel, M_{EPID}, is deconvolved using the dose scatter and glare kernel to produce in air fluence ϕ_{EPID}. The fluence is convolved with water scatter kernel, k_{water}, to generate a two dimensional dose distribution, D_{water}. 6
Figure 1-4: Flow charts of film based verification and EPID-based verification. It shows that the number of steps involved in each process. 7
Figure 2-1: Schematic of the head of a Varian Clinac 2100 EX 10
Figure 2-2: The flat panel EPID phantom model used in DOSXYZnrc and DOSRZnrc..... 11
Figure 2-3: 10mm two-dimensional picket fence test pattern 13
Figure 3-1: Depth response of the imager taken from 0 cm to 2.3 cm of water. The measurements are normalized to 0.4 cm. The error bars represent one standard deviation of the measurements. 14
Figure 3-2: The response of the flat panel EPID as a function of dose for a field size of 10x10 cm^2 15
Figure 3-3: The energy spectrum of the 6MV photon beam of Clinac 2100 EX calculated with BEAMnrc (solid) and the 6MV Mohan's spectrum is included for comparison (dotted). 16
Figure 3-4: A semilogarithmic plot of the spatial response of the scatter kernel of the flat panel EPID from a 6MV non-diverging pencil beam calculated with DOSRZnrc 17
Figure 3-5: flat panel EPID scatter kernel profiles of 6MV beam generated from Clinac 2100 EX (solid) and Mohan (dotted) spectra are shown. 18
Figure 3-6: The relative scatter factor, F(x), of the two 6MV scatter kernels. The 2100EX and Mohan are the $k_{s,base}$ and k_s respectively. 18
Figure 3-7 : Normalized profiles of flat panel EPID scatter kernels for 6MV (solid) and 15MV (dotted) beams. 19
Figure 3-8: Relative scatter factor, F(x), of 15MV beam relative to 6MV beam. The 6MV and 15MV are the $k_{s,base}$ and k_s respectively. 20
Figure 3-9: Scatter Kernel profile of the flat panel EPID (solid) with no build-up material and water phantoms (dotted) at a depth of 1.5 cm with 6MV beam..... 21
Figure 3-10: Relative scatter factor of water kernel relative to the flat panel EPID kernel at 6MV. The flat panel EPID kernel and water kernel are the $k_{s,base}$ and k_s respectively. 21
Figure 3-11: The deconvolution kernel in the frequency domain 22
Figure 3-12: (a) Test pattern captured using film; (b) test pattern captured using the flat panel imager 23
Figure 3-13: (a) Flat panel EPID and film profiles along the x-direction; (b) flat panel EPID and film profiles along the y-direction. 23
Figure 3-14: (a) Calibrated flat panel EPID and film profiles along the x-direction; (b) calibrated flat panel EPID and film profiles along the y-direction. 24
Figure I-1 This shows a schematic of a SLIC EPID. High voltage switches turn on the high voltage lines one at a time to turn on the horizontal array of ion chambers. The readings are read out via the electrometers which are muliplexed and sent to output via an amplifier. 32
Figure I-2: Video-based EPID consists of a video camera store connected to a video monitor outside the treatment room. A metal/phosphor screen is used for converting x-ray to visible light which is directed to the camera via a mirror. 33
Figure II-1 flat panel imager, EPID, measures a profile at Source to Detector Distance (SDD), M_{SDD}, which is back-projected to SAD to become M_{SAD}. 35

1. Introduction

1.1. Background

Intensity modulated radiation therapy (IMRT) is a form of conformal radiation treatment that uses sophisticated computer controlled high energy photon beam delivery to improve the conformity of the dose distribution to the shape of the tumor and to spare the surrounding normal tissue. This strategy improves local control of the tumor with lower normal tissue complications compared to conventional radiation treatment [1].

The first step in creating an IMRT treatment plan is to image the patient's internal anatomy to visualize and identify the tumor. This is typically done by computed tomography (CT) or with a combination of other techniques such as magnetic resonance imaging (MRI) or positron emission tomography (PET). Once the tumor target and the surrounding critical structures are identified and corresponding doses prescribed by a radiation oncologist, a medical physicist or delegate will use a computer optimization program to determine the number of beams, beam angles, beam shapes and intensity to best meet the criteria and goals.

The delivery of the intensity modulated radiation beam commonly relies on computer controlled multi-leaf collimators (MLC). MLCs are comprised of two banks of high atomic number metal leaves. Each leaf can be driven independently at different speeds by a motor. The dose conformity is achieved by a computer based treatment planning program that divides each field into a sequence of subfields. Each of these subfields has an assigned dose and an aperture which is set by the MLC. The number of subfields range from a few to over a hundred. Since the dose distribution of IMRT is a superposition of many apertures some of which could be very small, a few tenth of a millimeter uncertainty could result in several percents error for a 1 cm aperture [1] [2].

The complexity of IMRT also brings potential errors from each step throughout the process. Small errors in either the software or hardware along the process can be significant to the treatment outcome. For example, high local dose gradient which is common in IMRT can result in local hot/cold spots due to MLC misalignment or planning errors. Consequently, local tumor control failure or excessive normal tissue complications can occur [1] [2] [3]. The complexity also renders the IMRT plans to be impractical to check by manual calculation or single point verification measurement.

To address these new challenges, a set of new quality assurance (QA) procedures are recommended for IMRT [1] [4]. As part of a comprehensive IMRT QA program, the verification of delivered dose with planned dose is recommended, requiring some measurements of dose in two-dimensions. Radiographic film, because of their high spatial resolution and two-dimensional nature, are traditionally used for this purpose [1] [2] [5] [6]. Different types of electronic portal

imaging devices (EPID) have been shown to have potential to complement films [6] [7] [8]. The relative merits between EPID and films are discussed in the following sections.

1.2. Film Dosimetry

Film dosimetry for IMRT verification typically employs high resolution radiographic film (Kodak Ready Pack V2 or EDR2) combined with modern film density digitization. This provides an accurate and precise two-dimensional distribution from a single exposure [2]. The technique involves placing a film inside a polystyrene or Solid Water (commercially available, dosimetrically water-equivalent plastic) flat phantom at isocenter perpendicular to the beam axis with the gantry of the linear accelerator set at 0°. One film is used for each clinical field that is being verified. Film depth can vary from the depth of maximum dose (d_{max}) to 15cm depending on the depth of interest in the treatment plan. Pinholes are placed in the film marking the location of the cross-hair or points of registration. To calibrate the film used for the clinical fields, a set of calibration films, taken from the same batch of film, are exposed with known radiation field sizes, depth and doses to generate a calibration curve. The calibration curve is used to calibrate the optical density with the absolute dose giving a reproducibility of measured dose to within ~1%.
However, film suffers from several drawbacks [12]:

1. the dose response may be affected by processing conditions and production batch;
2. film verification of multiple fields is labour intensive;
3. film is an analog medium requiring digitization for quantitative comparison;
4. storage and archiving of films are inconvenient.

1.3. Electronic Portal Imaging Devices

Electronic portal imaging devices (EPID) are designed to operate in the megavoltage energy level between 1 and 20 MV [6]. They detect low energy electrons resulting from Compton scattering of high energy photons. To guage the efficiency of the imaging devices, a metric called detective quantum efficiency (DQE) is defined as,

$$DQE = \frac{SNR_{out}}{SNR_{in}} \qquad \textbf{(1-1)}$$

where SNR is the signal-to-noise ratio between the theoretical limitation of scattering and the system efficiency of the imaging device.
With the technological advancement in electronics, the image quality of EPIDs of various types has improved significantly. They can be classified into two types, direct and indirect detection. Both detectors have a build-up layer, typically a piece of thin copper, to convert high energy photons to secondary electrons. This layer also serves to filter out the contamination electrons from the head of the linear accelerator treatment unit. In the indirect case, an additional

scintillation screen is required to convert the secondary electrons to visible photons (see Figure 1-1a). Detectors are used to collect the optical photons. For the direct detector EPID, detectors are placed directly beneath the build-up layers (Figure 1-1b). Upon collecting the secondary particles in both the direct and indirect cases, a signal is generated and transferred for analysis via a set of peripheral electronics located around the device. Most imaging devices investigated by Boyer et al [6] fall short of the theoretical detective quantum limiting efficiency due to low conversion efficiency from one layer to the next. The challenge is to maximize the efficiency of each conversion to attain the quantum limited efficiency. Among all the approaches, only three can provide adequate information and are sufficiently practical to be commercialized and adopted clinically [7] [8] [9]. They are the scanning liquid ion chamber, the video-based, and the flat panel EPID. In this study, only the flat panel EPID will be discussed in detail in the following sections. More information of scanning liquid ion chamber and video-based EPID can be found in appendix Appendix I.

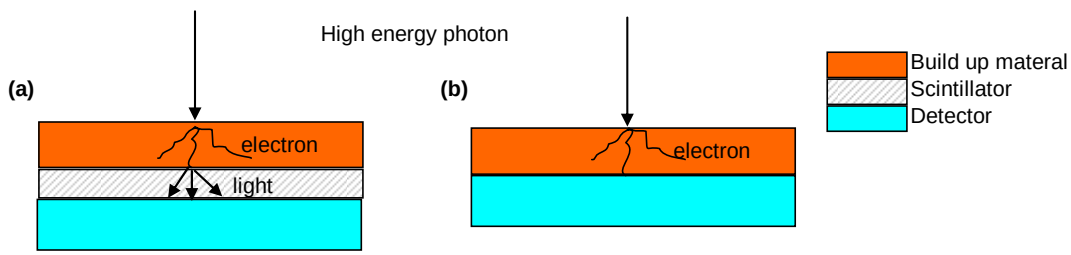

Figure 1-1: Two types of radiation detectors are shown here. (a) Indirect detector converts incident radiation into secondary electrons which are converted into visible light for detection; (b) Direct detector converts radiation directly into secondary electron for detection.

1.3.1. Flat Panel EPID

The flat panel EPID is an example of an indirect detector. This device is made from either amorphous silicon (a-Si) or amorphous selenium arrays. The system consists of a metal/phosphor combined build-up scintillation layer adhered to a flat panel detector and some peripheral electronics. Similar to video-based EPIDs, the metal/phosphor is used to generate light for detection. The flat panel EPID is fabricated essentially by the same technology as the liquid crystal display screen on a laptop computer. A thin layer of silicon is deposited on a thin glass (about 1mm) forming a two-dimensional thin film transistor (TFT) and photodiodes (Figure 1-2). Because of their high radiation tolerance, these integrated circuits can be placed directly in the radiation field in contact with the metal/phosphor plate forming a two dimensional detection array [6][7][8][9]. Each pixel of the flat panel is made up of a photodiode for light detection and a TFT for controlling the readout of the recorded signals. Image production in a pixel can be

summarized in a three-step process. The first step is pre-charge. The bias line is turned high to charge up all the photodiodes to pre-determined values. Entering the sampling cycle, the gate of the control field effect transistor (FET) at each pixel is kept low preventing any flow of current. The light, resulting from radiation hitting metal/phosphor screen, will discharge the photodiodes. During the readout cycle, the gates of the control FETs of each row of TFT will be turned on one at a time allowing charges to flow from the photodiode to the external amplifier via data lines for recording and analysis. The charge data is linearly proportional to the light reaching the photodiode during the irradiation. The readout rate for the entire array varies from 2 to 25 frames per second depending on the design of the readout electronics and the size of the array. The system efficiency is considered to be x-ray quantum limited and the spatial resolution is mainly determined by light spread in the phosphor screen [7] [8] [9]. Glare, which is defined as light scatter, is observed and is considered insignificant for imaging suggesting that a flat panel EPID is capable of producing high image quality[7][8]. However, for dosimetry, a 1-2% error in signal is significant enough to be considered [12] [10]. Its fabrication process allows a flat panel EPID to be made into different sizes providing another degree of flexibility. About 50% of the light emitted from the scintillator is used to produce the useful image which is orders of magnitude higher than other EPIDs (see Appendix Appendix I). This efficiency can be further improved in the future by adopting direct electron detection instead of the current indirect mode [8]. Radiation shielding of the electronics is required to avoid damage due to their close proximity to the detector. Additional quality assurance is still required to characterize its behaviour under various clinical environments [7].

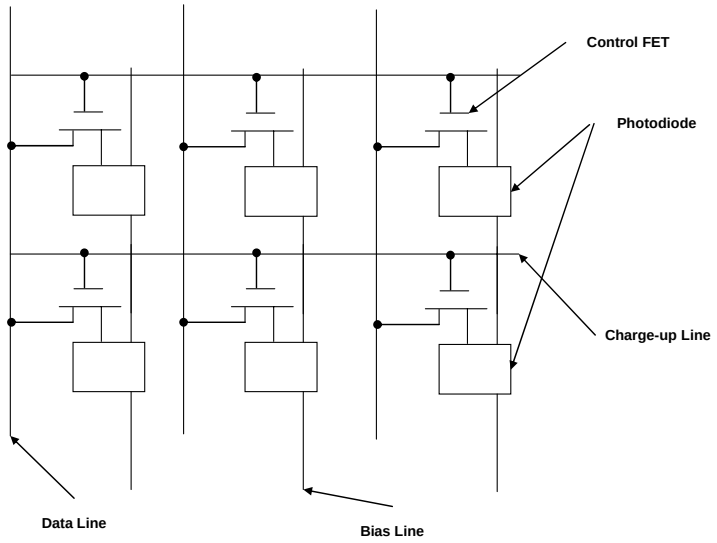

Figure 1-2: An array of photodiodes used for the flat panel imager is shown. Each photodiode collects visible photons generated by the high energy x-rays. The data are read out through the data line and the timing is controlled by the control FET. The bias line is used to control the bias to the photodiode and the charge-up line is used to control the opening and closing of the control FET.

1.3.2. Dosimetry

As the flat panel EPID is not water equivalent and has different scatter behaviour, it is important to calibrate the detector to dose measurement in water [10] - [20]. There are three methods that have been reported in the literature: an empirical method, a 2-step algorithm, and a deconvolution method. In this study, the main focus is on the deconvolution method and the rationale for this decision is given in the following sections. The empirical method and the 2-step algorithm are included in the appendix Appendix II for reference.

The flood field corrected raw pixel values, M_{EPID}, measured by the flat panel EPID can be modeled as a convolution of dose scatter kernel, k_s and glare kernel, k_g, with the incident photon fluence, ϕ as shown in the equation below:

$$M_{EPID} = (k_s \otimes k_g) \otimes \phi \qquad (1\text{-}2)$$

Instead of establishing a relationship between pixel value and dose, Warkentin [12] proposed the calibration of flat panel EPID using fluence. This method first deconvolves equation (1-2) using the calculated of k_s and k_g to determine incident photon fluence as shown in equation (1-3)

$$\phi = (k_s \otimes k_g) \otimes^{-1} M_{EPID} \qquad (1\text{-}3)$$

where

$\otimes^{-1}$	=	deconvolution operator;
M_{EPID}	=	flood field corrected raw image pixel values from flat panel EPID.

To determine the dose in another material, the calculated incident photon fluence is convolved with the calculated scatter kernel of the material of interest. For the purpose of radiation dosimetry, the material of interest is water which is considered to be tissue equivalent and the calculated dose in water is shown in equation (1-4) below:

$$D = h_{ic} \otimes \phi \qquad (1\text{-}4)$$

where

D	=	calculated dose distribution as measured by reference detector and
h_{ic}	=	scatter kernel of the calibration phantom.

The calculated value is compared with ion chamber measurement to establish the calibration factor. Figure 1-3 summarizes the procedure of converting the measurement from the flat panel imager to the dose in water.

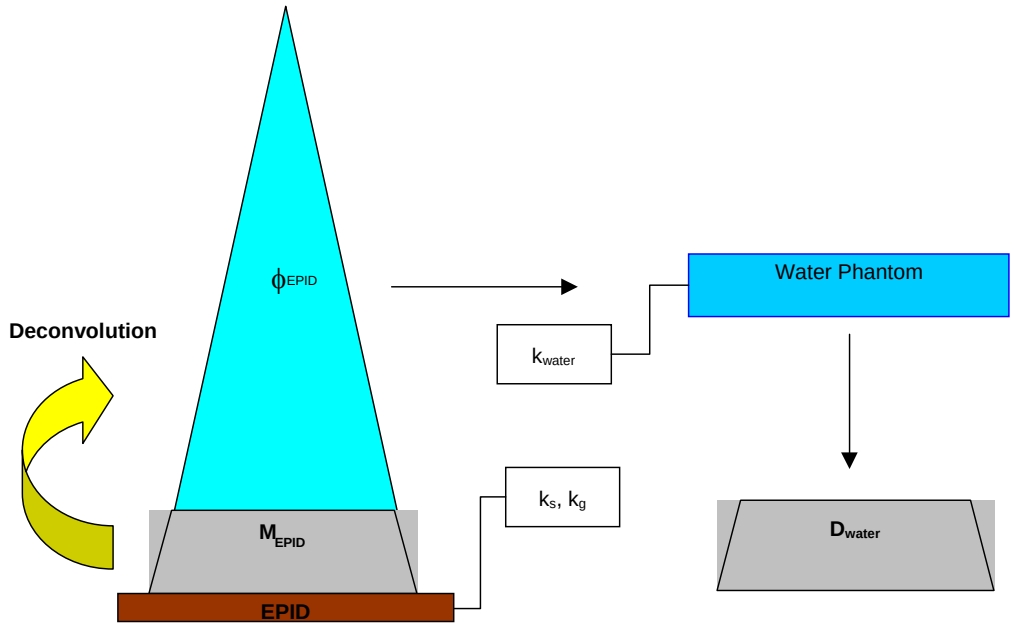

Figure 1-3: Measurement from the flat panel, M_{EPID}, is deconvolved using the dose scatter and glare kernel to produce in air fluence ϕ_{EPID}. The fluence is convolved with water scatter kernel, k_{water}, to generate a two dimensional dose distribution, D_{water}.

The advantage of this method is that it calibrates every point on the detector and eliminates the extra step of determining the phantom scatter factor to account for off-axis behaviour. Since the photon fluence is determined directly from the measured data of flat panel, no new calculation is required for a new field of verification. To obtain the dose distribution inside any target phantom, the deconvolved photon fluence is convolved with the scatter kernel of the phantom. No back-projection operation is necessary resulting in faster operation. Despite the high computation time for calculating the phantom kernel using Monte Carlo simulation, this only needs to be calculated once. A measured 2D dose distribution has been demonstrated to provide good agreement with film and ion chamber [12]. The linear convolution character of this method enables the possibility of 3D dosimetry. On the verification, there is no existing method of direct measurement of photon fluence to assess the accuracy of the calculated results. To tackle this problem, the use of a diamond detector was proposed to measure pseudo fluence for verification purposes [12]. Also, Warkentin's flood field calibration factor requires calibrating the flat panel EPID at every depth due to the use of varying reference depths.

Based on the literature review discussed above and in appendix Appendix II, the deconvolution method suggested by Warkentin [12] provides the best potential for two-dimensional dosimetric application.

1.4. Film and Portal Imaging Workflow Comparison

Traditionally film is considered to be the "Gold Standard" for two-dimensional dose verification for IMRT. However, the use of film requires several hours of work for each patient-specific quality assurance procedure. For example, a typical IMRT plan may consist of 6 to 8 treatment fields, each requiring separate exposures in addition to several calibration exposures which typically requires about 2.5 hours [12]. In addition to this, the film processing procedure must be carefully controlled to minimize the batch and process dependence. After processing, unlike the EPID which is already in digital format, film has to be digitized before quantitative dose analysis can be carried out. With the increasing amount of film required for IMRT verification, archiving and storage of processed film requires significant storage space while digital output of EPID system may be stored onto compact digital media.

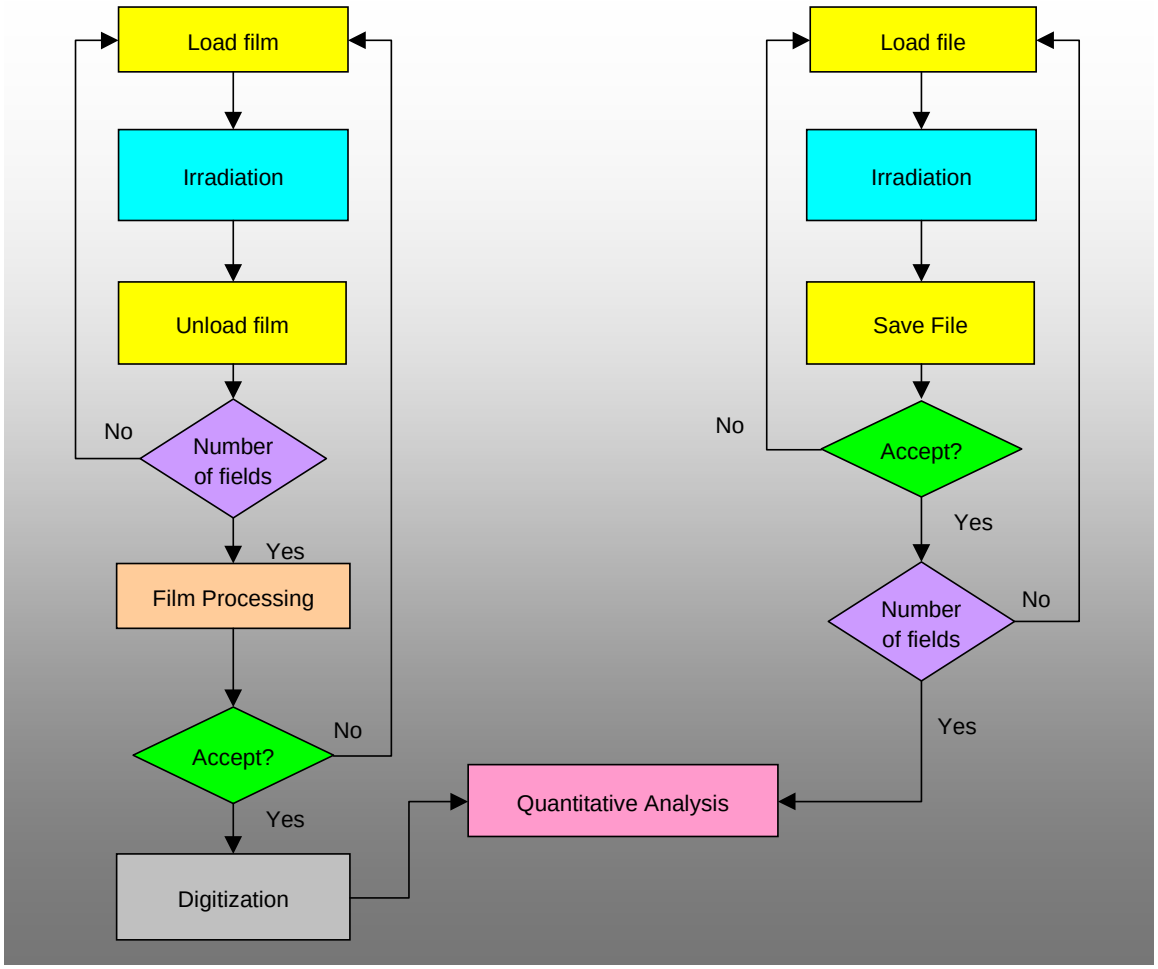

Figure 1-4: Flow charts of film based verification and EPID-based verification. It shows that the number of steps involved in each process.

1.5. Motivation

With the increasing use of intensity modulated radiation therapy incorporating beams with complex fluence distributions, the requirement for two-dimensional dose verification is expected to increase. Although conventional film dosimetry is adequate this purpose, the shorter workflow of flat panel EPID with proper calibration promises to reduce the manpower required for this task. To understand the feasibility of using this device in IMRT verification, the dosimetric behaviour of the device must be established.

2. Method

A series of tests were designed to understand the dosimetric behaviour of the detector. All measurements in this thesis were collected on a Varian Clinac 2100 EX linear accelerator with a 6MV photon beam and an amorphous silicon, flat panel imager at a source to surface distance (SSD) of 140 cm. The equivalent build-up depth and dose response of the detector were measured. To calibrate the detector, the scatter kernel, k_s, was calculated using BEAMnrc and EGSnrc Monte Carlo simulation routine [22] [23] [24] [25]. Verification of the calculated scatter kernel was accomplished by comparing the results with published data. To verify the behaviour of the calibration method, a 1 cm wide picket fence IMRT test pattern was used.

2.1. Equivalent Build-up Depth

The EPID was irradiated with a field size (FS) of 10x10 cm^2, an energy of 6 MV and 100 monitor units (MU). Different thicknesses of Solid Water slabs were added systematically at each irradiation to obtain the response of the detector at different depths. The results were compared with the percent depth dose commissioning data of the beam after adjusting for the increased source-detector distance using the inverse square using the equation below.

$$\phi_1 = \phi_2 \frac{f_2^{\,2}}{f_1^{\,2}} \qquad (2\text{-}1)$$

where ϕ_1 and ϕ_2 are the fluence at distances f_1 and f_2 respectively [17]. The results were normalized to the maximum measured value and compared to the commissioning data. The lateral shift displacement of the two curves is taken to be the equivalent build-up depth.

2.2. Dose Linearity Response

To investigate the pixel response with dose, the imager was exposed to doses ranging from 10 to 300 cGy at a dose rate of 300cGy/min. The machine was calibrated to 1cGy per 1 monitor unit (MU) at d_{max} for a source-axis-distance (SAD) of 100 cm and FS = 10x10 cm^2. Five pixels of each measurement from the imager at the beam center were averaged to represent the response. Three measurements were made at every dose point to establish a reasonable statistics and reproducibility.

2.3. Scatter Kernel Determination

The determination of the scatter kernel involved Monte Carlo simulations using BEAMnrc and EGS4 routine [22] - [25]. The energy spectrum and the phase space file of the x-ray beam were first generated in BEAMnrc. As the field size used is small (0.784 x 0.784 cm^2), the electron contamination effect is insignificant and we uses an energy spectrum to generate the scatter kernel instead of the more rigorous phase-space file which would be required for much larger field

sizes. The spectrum was then fed into DOSXYZnrc and DOSRZnrc routines of EGS4 to calculate the scatter kernels of the specified phantoms. The kernels were verified by comparing a kernel generated using Mohan's [27] spectrum.

2.3.1. 6MV X-ray Beam Energy Spectrum Simulation

The head of the Clinac 2100EX linear accelerator was first modeled in BEAMnrc. The schematic of the head of the accelerator is shown below [26].

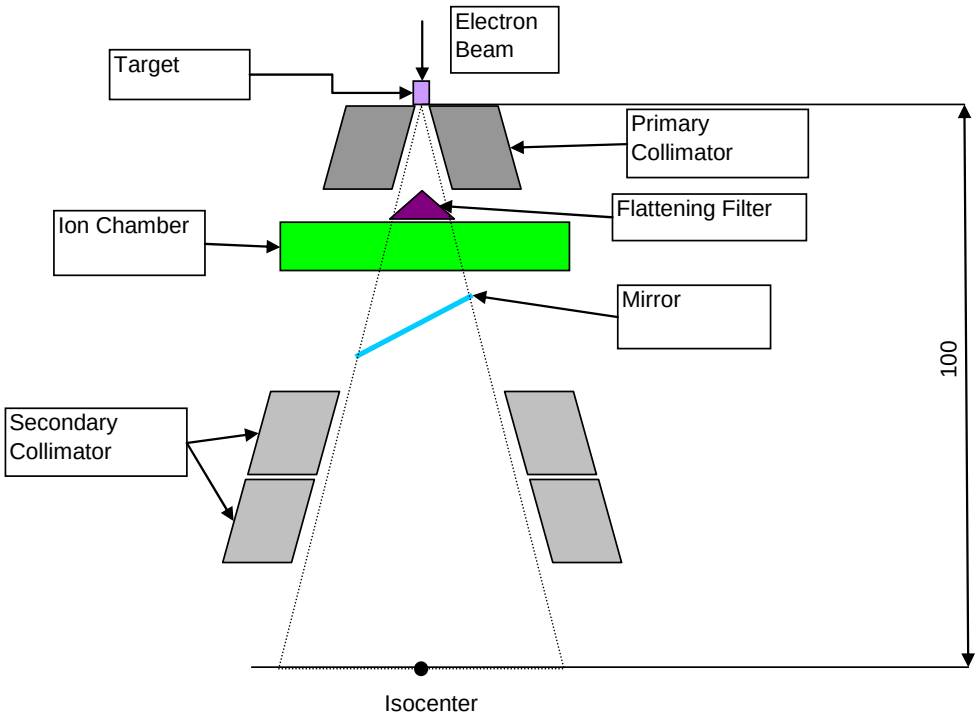

Figure 2-1: Schematic of the head of a Varian Clinac 2100 EX

The initial energy of the electron beam striking the target was set at 6MeV with a history and field size of $1x10^9$ particles and 10x10 cm^2 respectively using the BC Cancer Agency's Monte Carlo simulation cluster. The scoring plane was at a distance of 100 cm from the target.

2.3.2. Scatter Kernel Simulation

The scatter kernel was determined by calculating the energy deposition distribution from irradiating a pencil beam onto a phantom. The pencil beam was modeled as a non-diverging beam of 0.784x0.784 mm^2 field size using the simulated photon energy spectrum from the previous section. This profile was fed into DOSXYZnrc and DOSRZnrc routines to generate energy deposition in the flat panel EPID, film and water phantoms with a history in the range of $1x10^8$ to $1x10^9$ particles.

The phantom used in this simulation has a size of 40x40 cm^2 to allow sufficient lateral electron scattering. A published phantom model [12] of the imager for Monte Carlo simulation was used in the calculation and shown below:

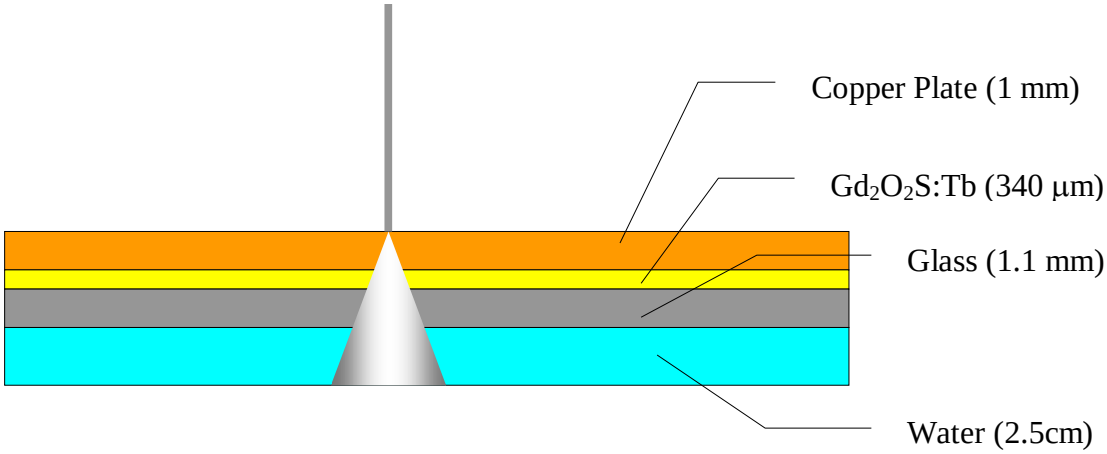

Figure 2-2: The flat panel EPID phantom model used in DOSXYZnrc and DOSRZnrc

By simulating the irradiation of the pencil beam onto the phantom, the 2-D dose deposition profiles at different scoring planes were obtained. The scoring plane to model the energy deposition of a photon onto the scintillation layer where low energy light emitted was chosen at the bottom of the scintillation layer. The scatter of the lower energy light was modeled using a previously published glare kernel [12].

2.4. Verification

Once the scatter kernel of the flat panel EPID was generated, it was first verified through a series of parametric variations in spectrum, energy and phantom materials. It was also verified through experimental measurements by comparing calibrated flat panel EPID measurement to the film measurement as described below.

2.4.1. Verification of Monte Carlo Calculation

To quantify the difference between calculated scatter kernels, a relative scatter factor, *F(x)*, was defined as the percentage change in magnitude between the kernels at the same distance, *x*, from the center of the beam. It was shown as follows:

$$F(x) = \frac{k_s(x)}{k_{s,base}(x)} - 1 \qquad (2\text{-}2)$$

where $k_{s,base}$ and k_s are the base scatter kernel and kernel of interest respectively. The positive value of $F(x)$ means that $k_s(x)$ has more scatter than $k_{s,base}(x)$ at that point.

2.4.1.1. Spectrum

For comparison purpose, a 6MV spectrum published by Mohan [27] was used to generate another scatter kernel of a flat panel EPID using the DOSXYZnrc and DOSRZnrc at the same scoring plane. The relative scatter factor was dictated by the mean energy of the beam. The higher the mean energy of the beam should deliver lower amount of the scattered photons. This translates to lower value in scattering kernel.

2.4.1.2. Energy Effect

The 6MV and 15MV energy spectra of the Varian Clinac 2100 EX linear accelerator and Mohan's published data [27] were used respectively to generate two scatter kernels in the flat panel EPID. In both cases, no build-up material was used. Because of the higher energy of the 15MV beam, it is expected that the results from this beam will exhibit less scattering.

2.4.1.3. Phantom Material

In this part of the study, a 6MV Clinac 2100 EX beam was used. The phantom materials of water at a depth of 1.5 cm and flat panel EPID with no build-up material were used to generate two scatter kernels. Because of higher atomic number of the flat panel EPID, it is expected to have higher amount of scatter.

2.4.2. Experimental Verification

After verifying the calculation, the flat panel EPID scatter kernel was used to generate a deconvolution kernel for calibration purpose. To assess the effectiveness of the calibration, a 1.0 cm picket fence pattern was used as a test pattern [1]. The calibrated flat panel EPID measurement was registered and compared to the film measurements.

2.4.2.1. Deconvolution Kernel

Using the scatter kernel generated in the previous section and the glare kernel from publication [12], a two-dimensional convolution kernel was obtained by rotating the one dimensional scatter kernel calculated in the previous section. The deconvolution kernel was calculated from the reciprocal of the two-dimensional kernel in the frequency domain.

2.4.2.2. Test Pattern

A 1.0 cm wide picket fence pattern leaf motion file was created in the MLC Shaper program. This leaf motion file was transferred to multi-leaf collimator controller of the 2100 EX linear accelerator which programmed the multi-leaf collimator to deliver the test pattern. Figure 2-4 below shows the beam's eye view of the test pattern.

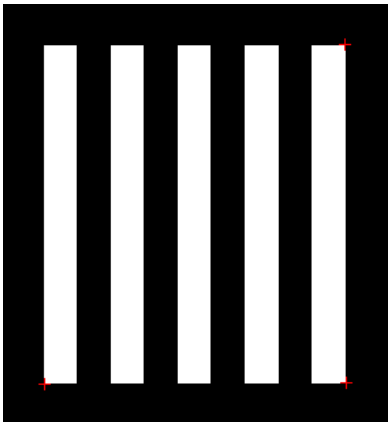

Figure 2-3: 10mm two-dimensional bar pattern test pattern

The high dose gradient in the pattern tests the high spatial frequency reproducibility of the film and the flat panel imager.

2.4.2.3. Comparison

Kodak EDR2 radiographic film was used as a benchmark to assess the performance of the deconvolution method. Each film was placed inside a Solid Water phantom with 2 cm of build-up material and 12 cm of backscatter materials. The assembly was then placed at a source to film distance of 140 cm. During each experiment, all the films were taken from the same batch to minimize film variation. At the end of each set of measurements, the exposed films are processed at the same time to minimize process variation. The measurements were digitized for analysis using a Vidar 16 scanner.

The flat panel EPID measurements were registered to the films using the three corners of the test pattern (Figure 2-3). The agreement of the radial and transverse profiles of the measurements of the EPID and the films were compared before and after applying the calibration to assess the effectiveness of the calibration. All the comparisons were normalized to the center of the field in this study. Several analysis tools were written in MATLAB to register, normalize, generate and compare dose profiles from the acquired film and imager data. The programming codes are included in the Appendix III.

3. Results

3.1. Inherent Water Equivalent Build-up Thickness

Figure 3-1 shows the response of the detector with different Solid Water build-up thickness. The curve is normalized to the measurement at depth of 0.4 cm.

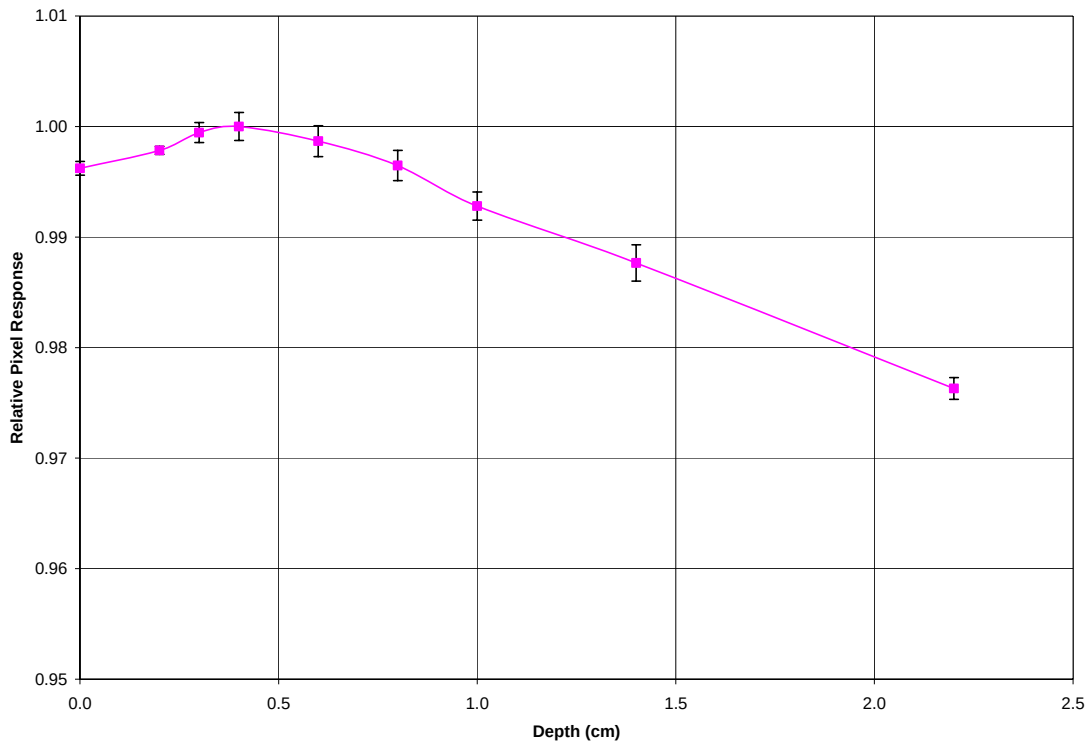

Figure 3-1: Depth response of the imager taken from 0 cm to 2.3 cm of water. The measurements are normalized to 0.4 cm. The error bars represent one standard deviation of the measurements.

3.2. Dose Linearity Response

The open field response curves of the flat panel imager are shown in Figure 3-2. The measurements are the average value of the pixels in an area of 1.0 x 1.0 cm^2 at the central axis. The least square fitted linear curve has a slope of 6.82 with correlation coefficient, R^2, of 1.00. The first standard deviation of the measurements is about 0.3%.

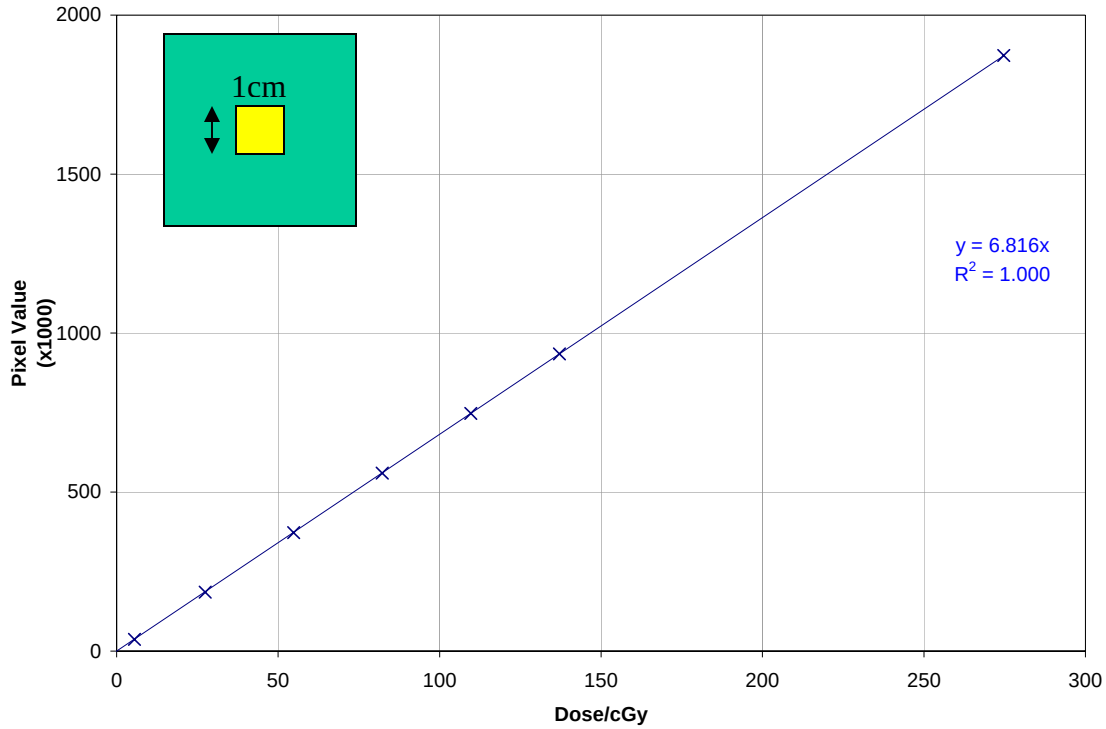

Figure 3-2: The response of the flat panel EPID as a function of dose for a field size of 10x10 cm^2

3.3. Scatter Kernel

The results of the 6MV energy spectrum of 2100 EX and the corresponding scatter kernel for the flat panel EPID generated from the Monte Carlo simulations are presented in this section. The input files relating to the simulations are included in the Appendix Appendix IV.

3.3.1. 6MV X-ray Beam Energy Spectrum

The 6MV photon beam for Clinac 2100 EX was simulated. The energy spectrum of the results was calculated and is shown in Figure 3-3. The solid line and dotted line represent the 2100 EX and Mohan spectra respectively with different mean photon energy.

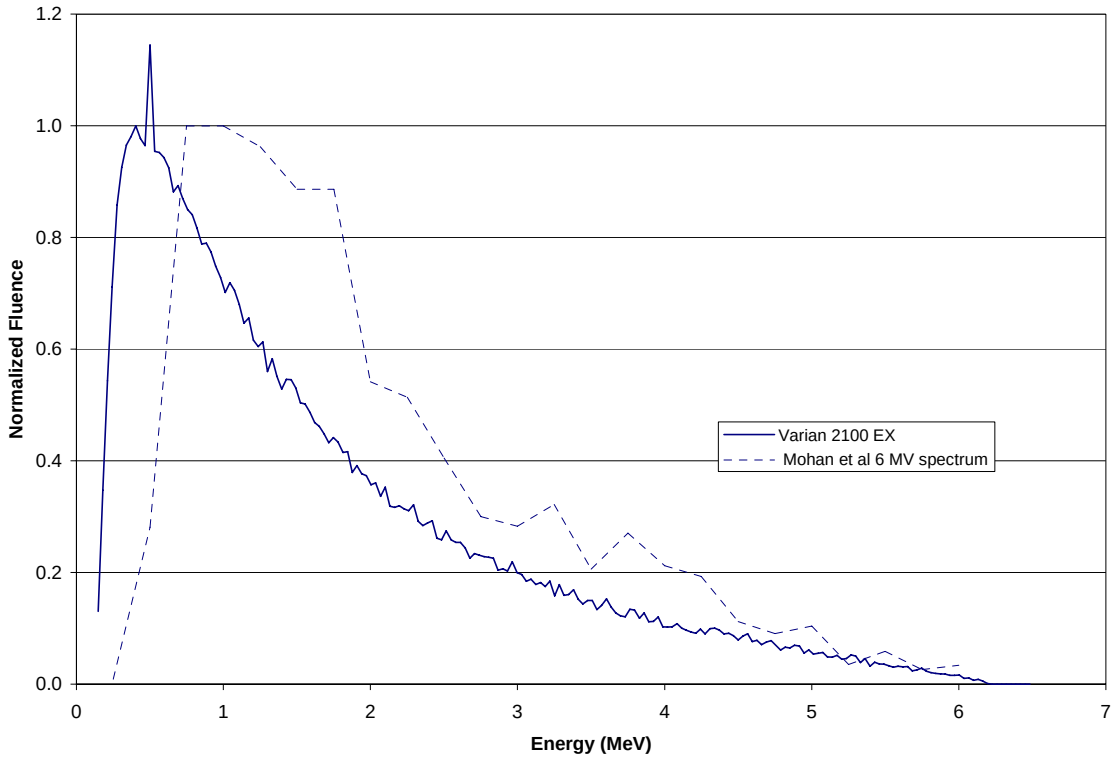

Figure 3-3: The energy spectrum of the 6MV photon beam of Clinac 2100 EX calculated with BEAMnrc (solid) and the 6MV Mohan's spectrum is included for comparison (dotted).

3.3.2. Scatter Kernel Simulation

Using the energy spectrum obtained in the previous section, the scatter kernel of the flat panel EPID was calculated in DOSRZnrc. Figure 3-4 shows the calculated flat panel EPID scatter kernel. The kernel is normalized with the maximum value at the central axis of beam. The x-axis depicts the distance from the central axis of the photon beam.

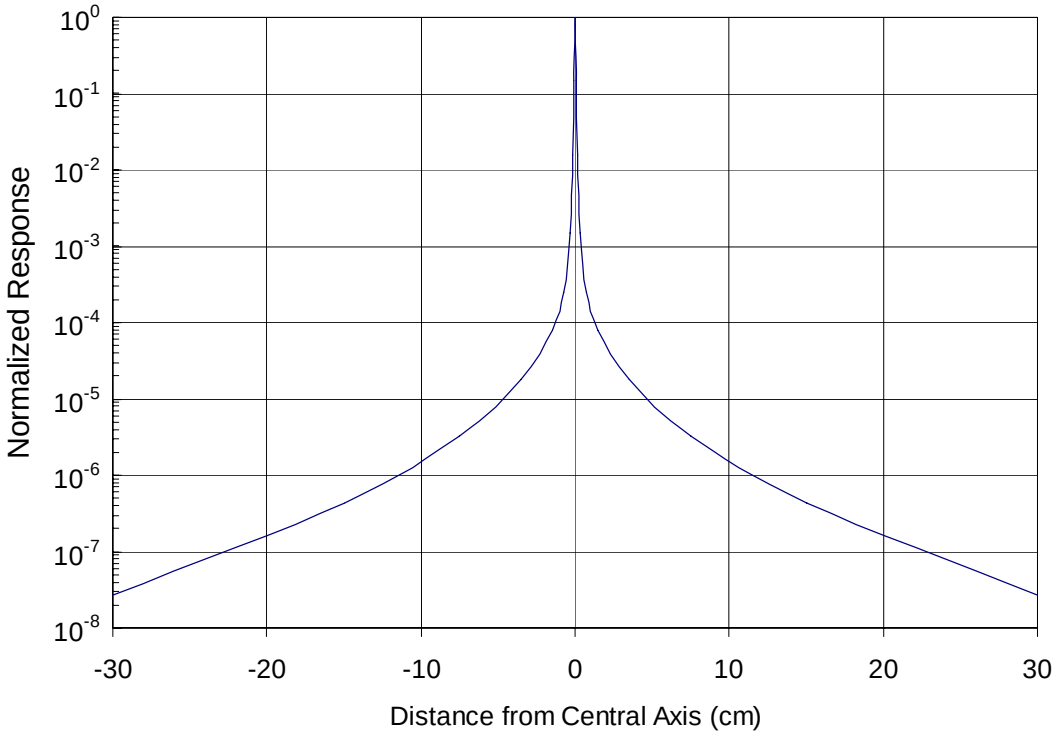

Figure 3-4: A semilogarithmic plot of the spatial response of the scatter kernel of the flat panel EPID from a 6MV non-diverging pencil beam calculated with DOSRZnrc

3.4. Verification

3.4.1. Verification of Monte Carlo Simulation

In this section, the results from the calculation of spectrum, energy and phantom effects are presented. In each of the three sections, a plot of scatter kernel response and a plot of the corresponding relative scatter factor response are presented.

3.4.1.1. Spectrum Effect

The flat panel EPID scatter kernels from two different spectra of 6MV photon beam are presented in Figure 3-5. The two spectra are of Clinac 2100 EX (solid) and Mohan (dotted). Figure 3-6 shows the relative scatter factor of the two scatter kernels shown in Figure 3-5. The $k_{s,base}$ and k_s used in this plot are the 2100EX and Mohan kernels respectively.

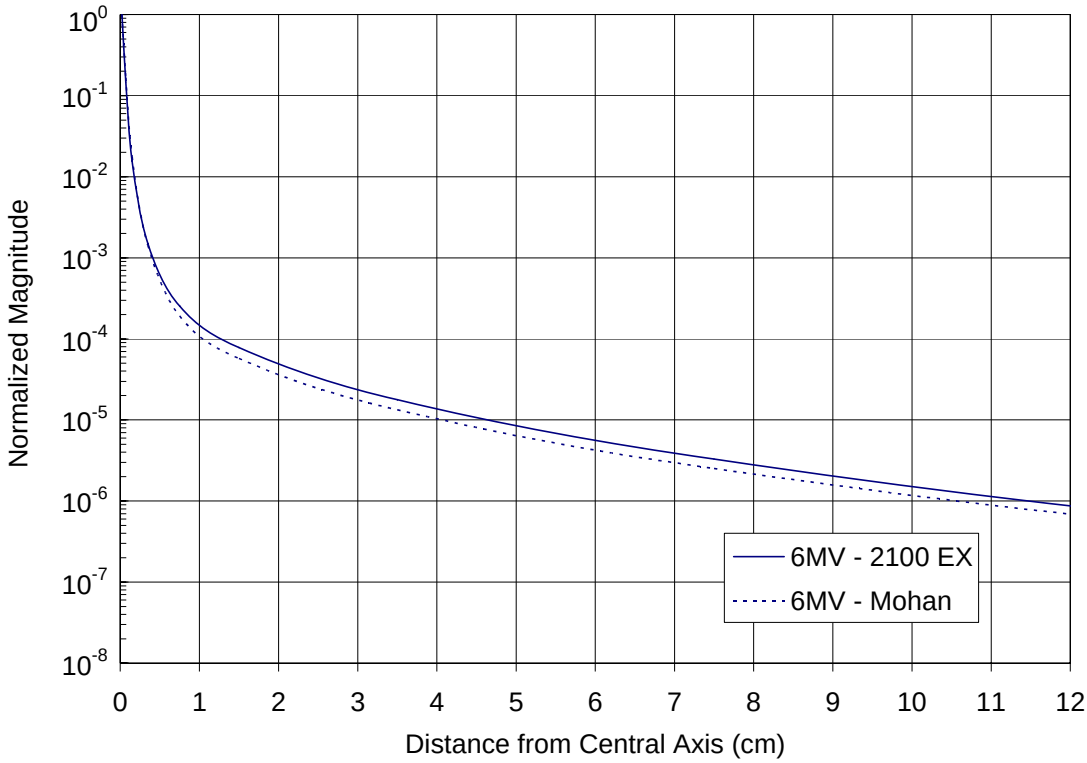

Figure 3-5: EPID scatter kernel profiles of 6MV beam generated from Clinac 2100 EX (solid) and Mohan (dotted) spectra are shown.

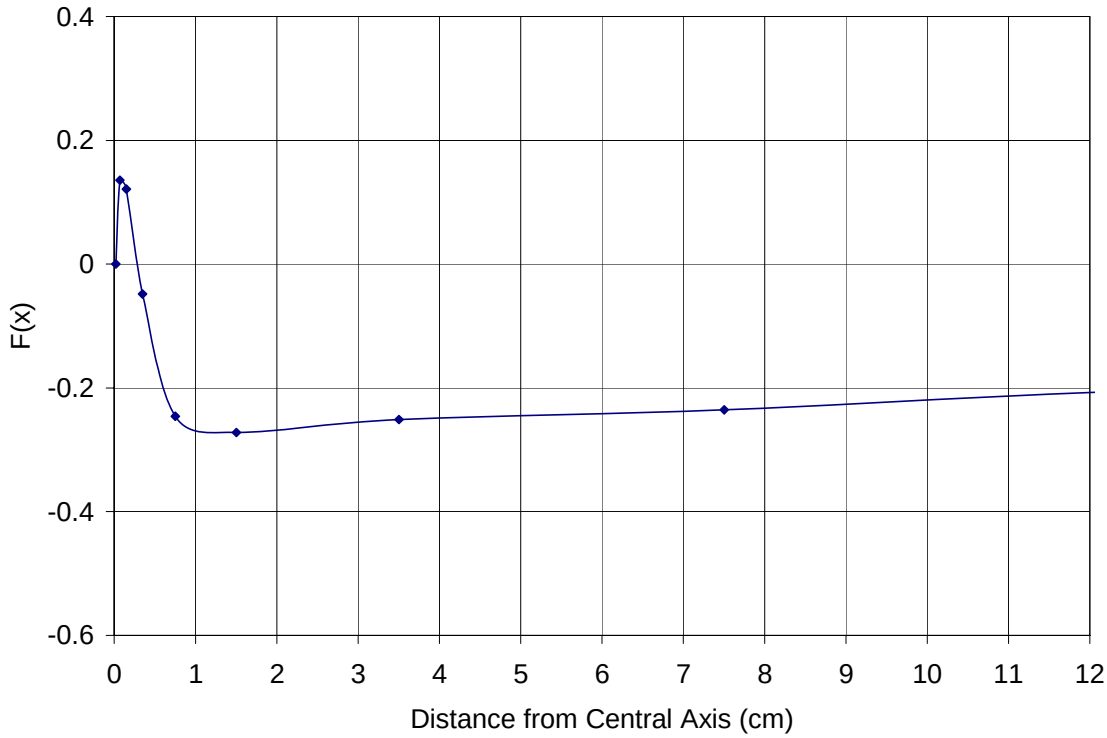

Figure 3-6: The relative scatter factor, F(x), of the two 6MV scatter kernels. The 2100EX and Mohan are the $k_{s,base}$ and k_s respectively.

3.4.1.2. Energy Effect

The flat panel EPID scatter kernel of a 6MV and a 15MV beams with the energy spectrum of Clinac 2100EX and Mohan's data [27] respectively are presented in Figure 3-7. Figure 3-8 shows the relative scatter factor of the two energies. Here, the k_s is the 15MV beam.

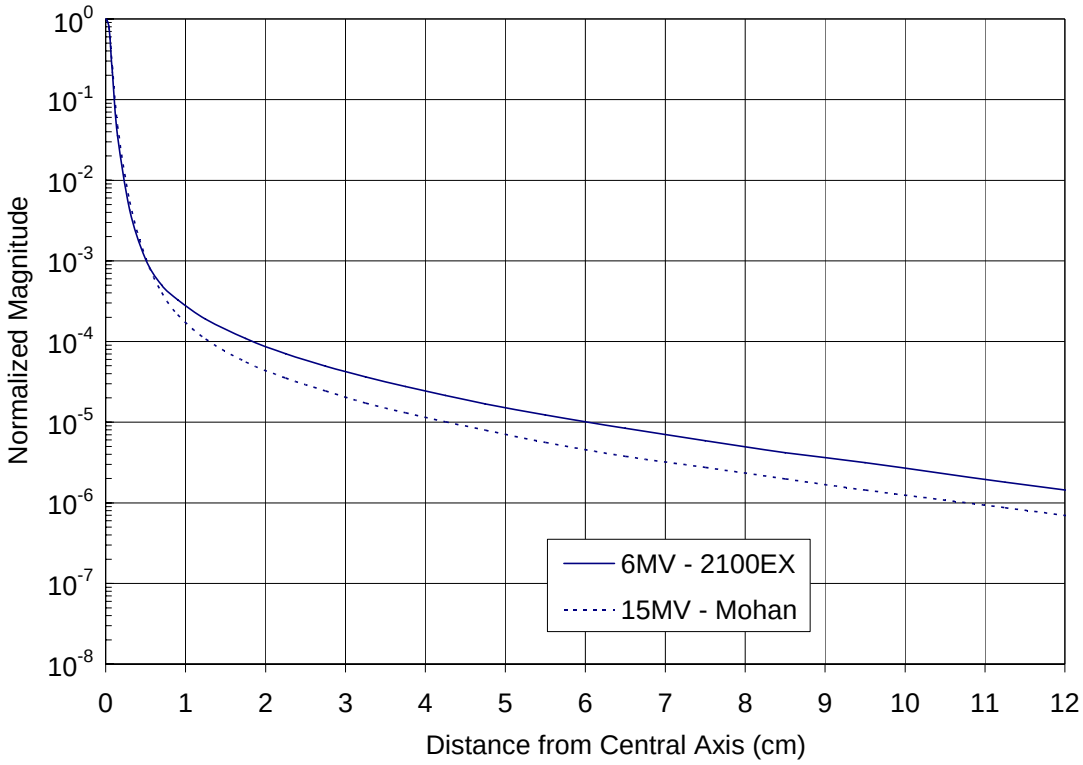

Figure 3-7 : Normalized profiles of flat panel EPID scatter kernels for 6MV (solid) and 15MV (dotted) beams.

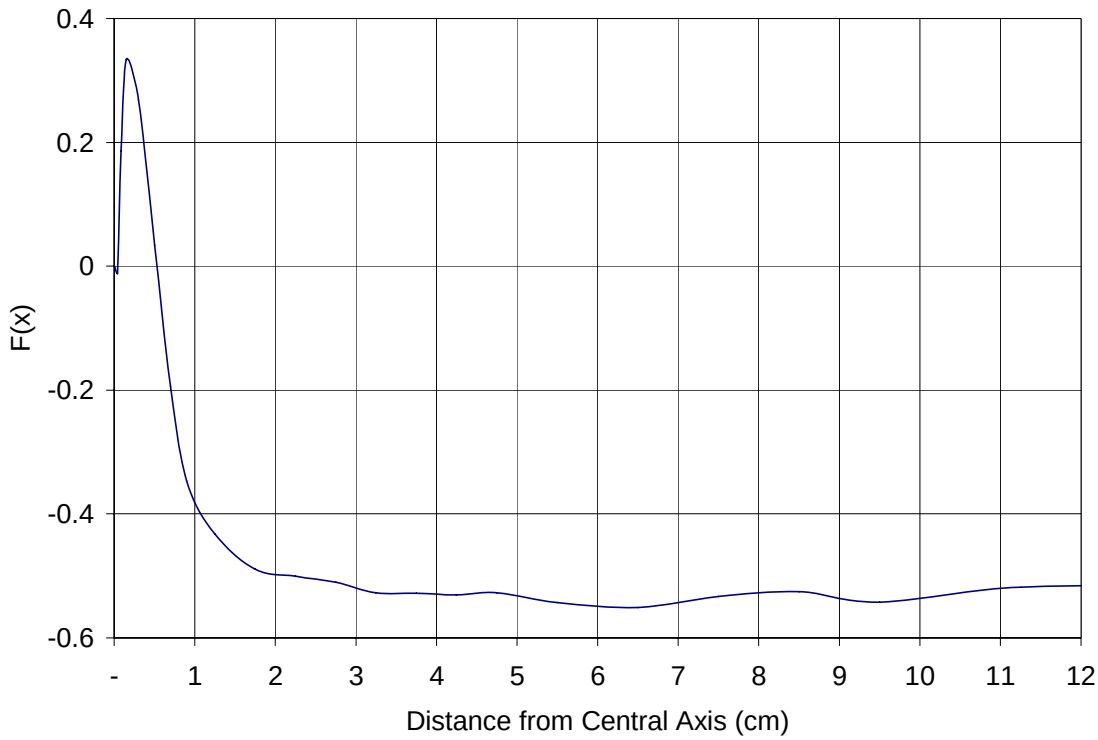

Figure 3-8: Relative scatter factor, F(x), of 15MV beam relative to 6MV beam. The 6MV and 15MV are the $k_{s,base}$ and k_s respectively.

3.4.1.3. Phantom Material

Figure 3-9 shows the effect of phantom material on scatter kernel generated using the 21EX spectrum at 6MV. The water scatter kernel is calculated at a depth of 1.5 cm. Figure 3-10 shows the relative scatter factor plot with $k_{s,\,base}$ and k_s being the flat panel EPID and water scatter kernel respectively.

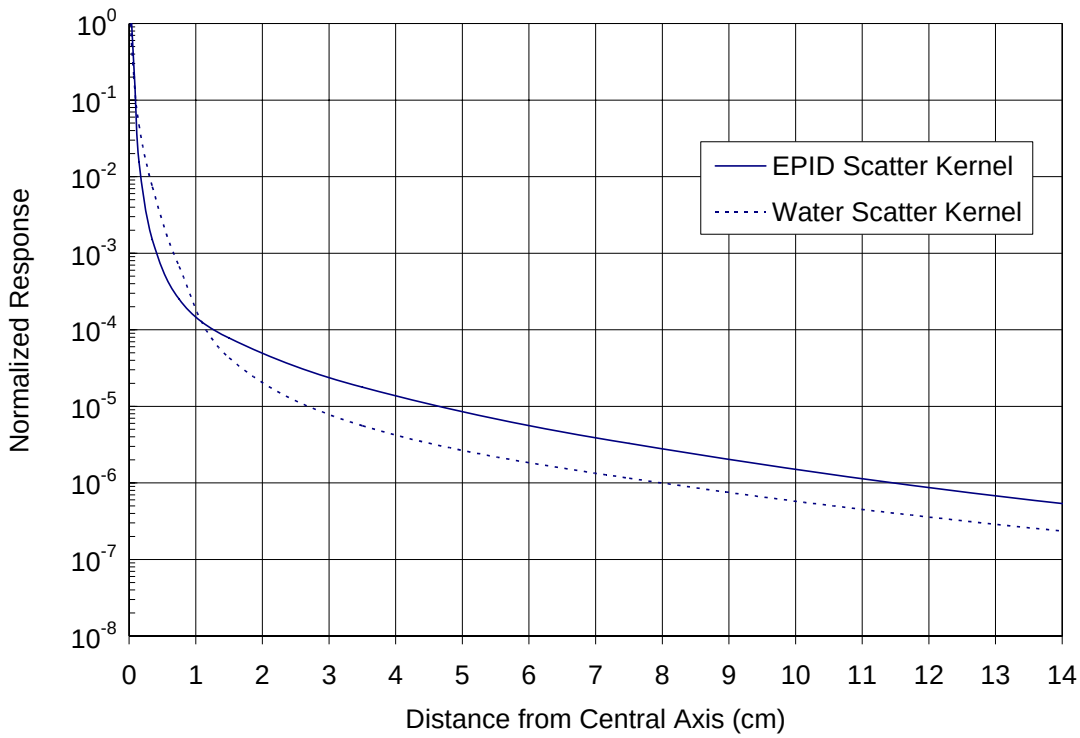

Figure 3-9: Scatter kernel profile of the flat panel EPID (solid) with no build-up material and water phantoms (dotted) at a depth of 1.5 cm with 6MV beam

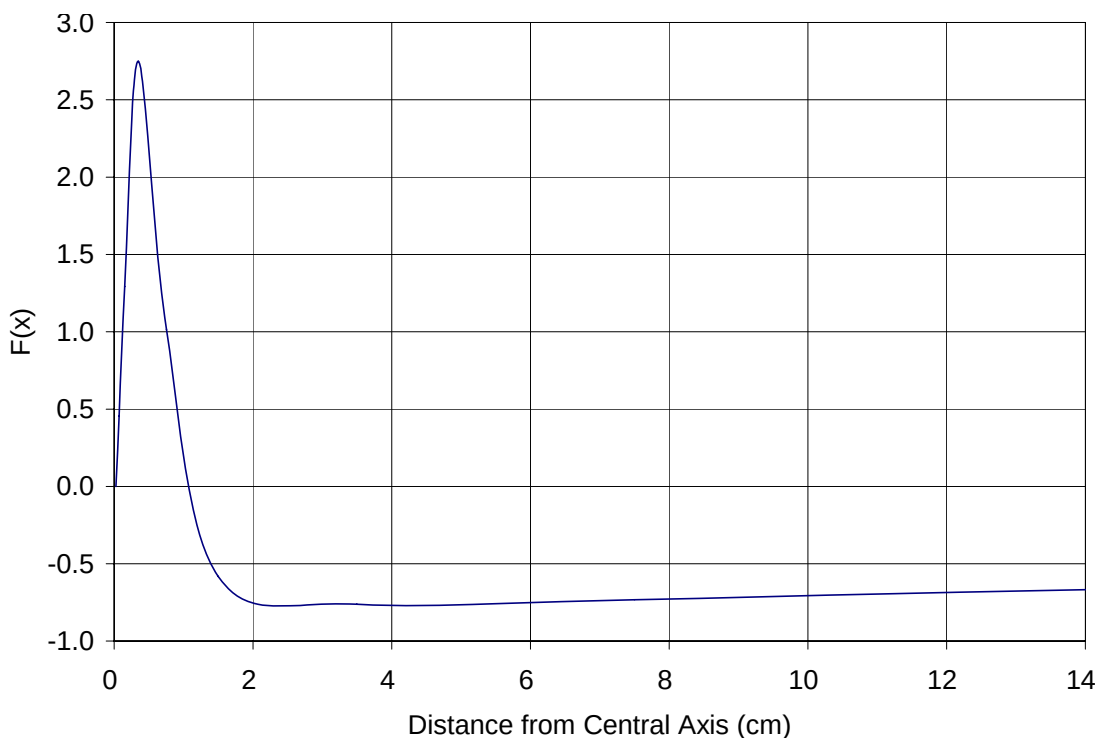

Figure 3-10: Relative scatter factor of water kernel relative to the flat panel EPID kernel at 6MV. The flat panel EPID kernel and water kernel are the $k_{s,base}$ and k_s respectively.

3.4.2. Experimental Verification

In this section, the comparison of the relative dose obtained from the flat panel imager and film in a water phantom are discussed.

3.4.2.1. Deconvolution Kernel

The deconvolution kernel was generated and is shown in Figure 3-11.

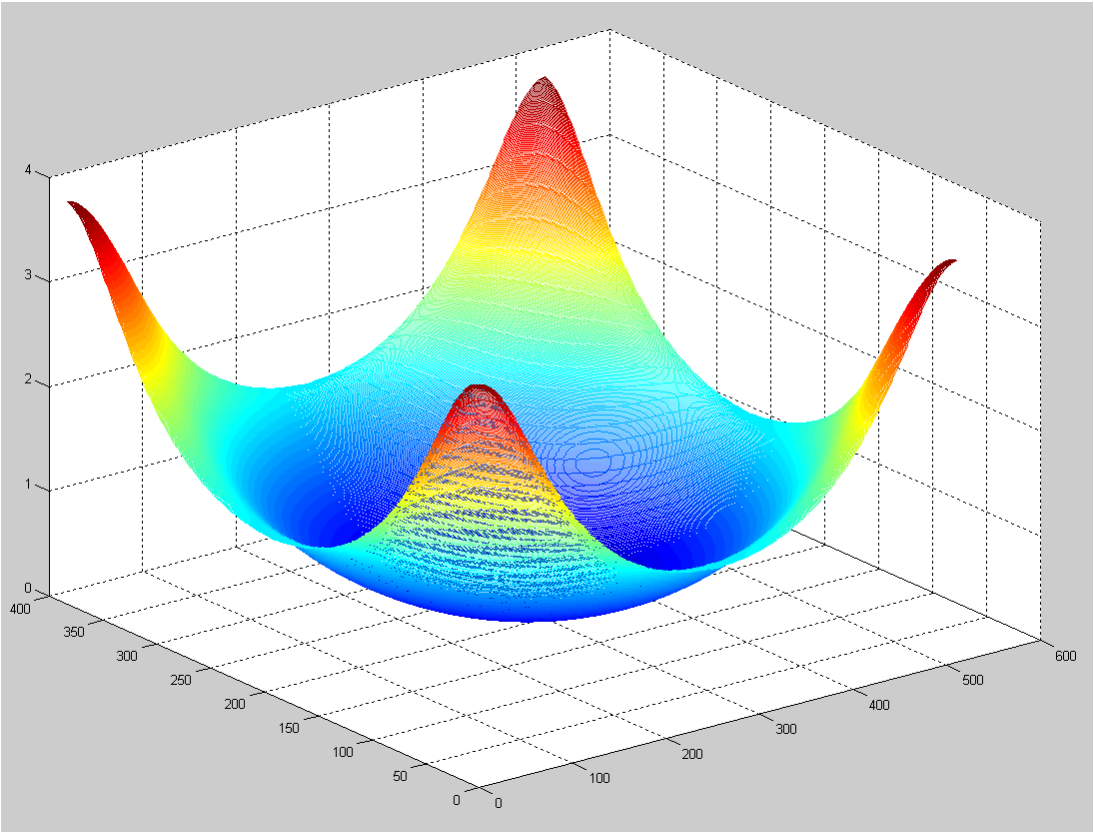

Figure 3-11: The deconvolution kernel in the frequency domain

.

3.4.2.2. Test Pattern

The test pattern used in the investigation is a 10mm bar pattern. Figure 3-12 shows the images captured using film and the flat panel imager

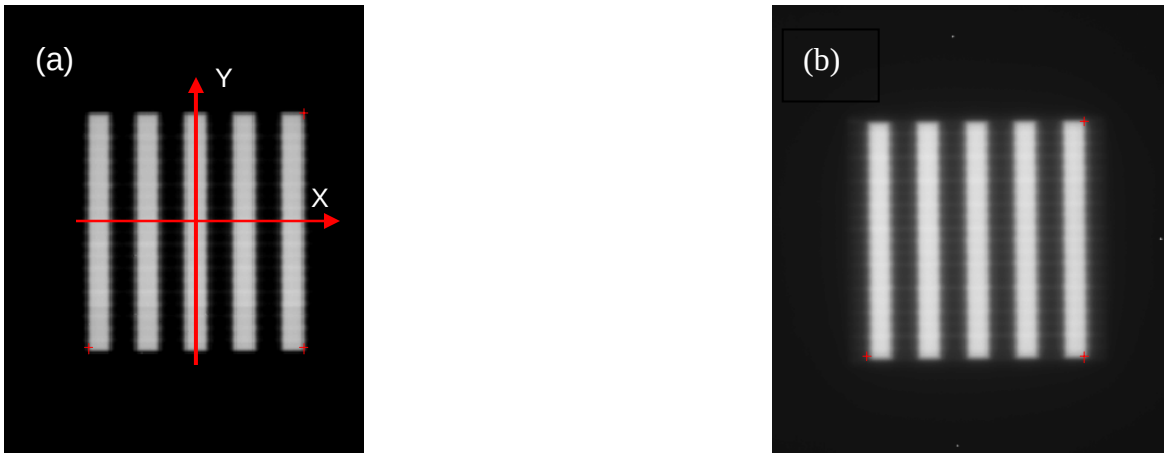

Figure 3-12: (a) Test pattern captured using film; (b) test pattern captured using the flat panel imager

3.4.2.3. Profile Comparison

The relative dose profiles along transverse and longitudinal directions are denoted as x and y directions (Figure 3-12). Figure 3-13 shows the profiles captured from film (dotted) and the flat panel imager (solid) along x and y direction before the calibration. The profiles are normalized at the center of the test pattern. Figure 3-14 shows the same profiles after calibration.

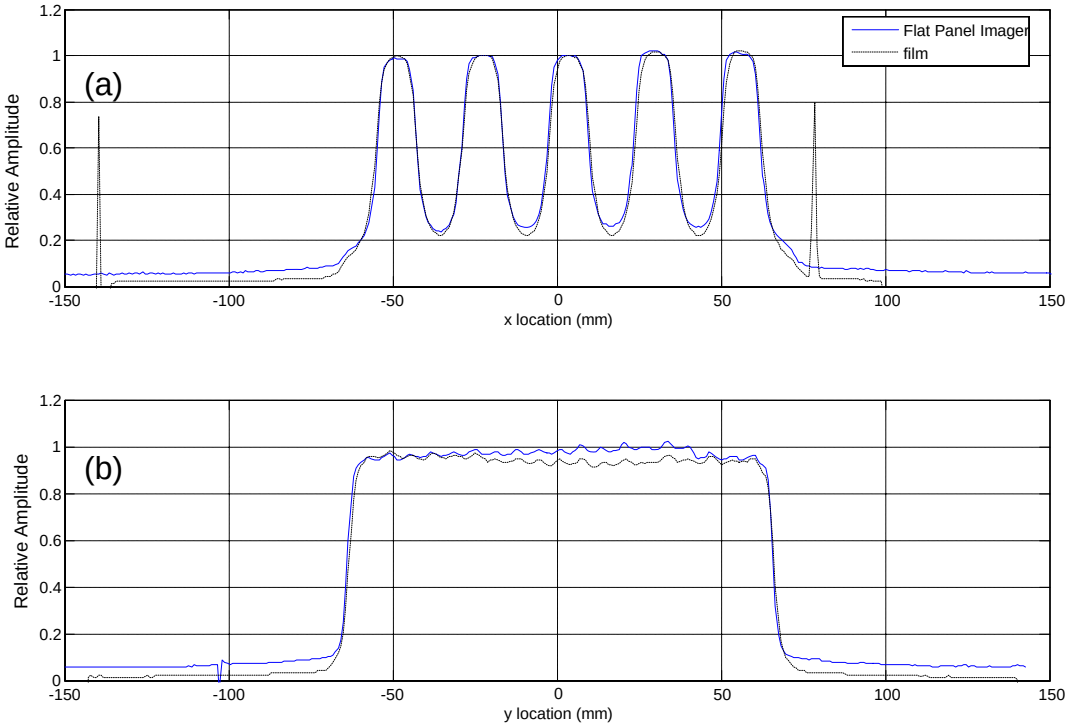

Figure 3-13: (a) Flat panel EPID and film profiles along the x-direction; (b) flat panel EPID and film profiles along the y-direction.

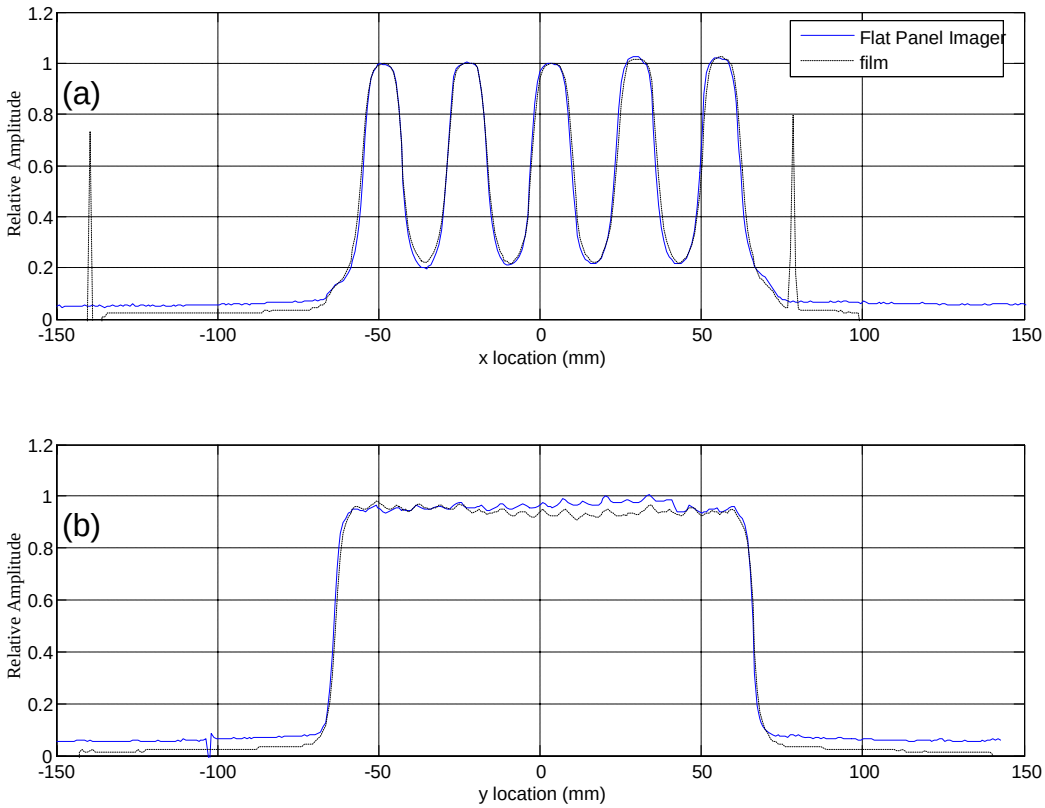

Figure 3-14: (a) Calibrated flat panel EPID and film profiles along the x-direction; (b) calibrated flat panel EPID and film profiles along the y-direction.

4. Discussion

4.1. Inherent Water Equivalent Build-up Thickness

Beyond the depth of 0.4cm, the response decreases with the addition of water implying that the electronic equilibrium has been reached (Figure 3-1). With the knowledge that the maximum dose response of 6MV occurs at the depth of 1.5 cm of water, we have deduced that the flat panel imager has an inherent water equivalent build-up of 1.1 cm.

Comparing the magnitude of the peak and the case without build-up, the difference is less than 0.5%. For clinical applications with an acceptable error margin of 2%, it is sufficient that the imager is used as-is without any build-up material.

4.2. Dose Linearity Response

The correlation coefficient from the least square fitting yields a value of 1.00 with about 0.3% of uncertainty. This shows that the response of the imager has a linear response with dose in the range between 0 to 300 cGy.

4.3. Scatter Kernel

The response of the scatter kernel falls rapidly with increasing distance from the center. Within 5 centimeters from the point of irradiation, the simulation shows that the response has a drop of more than 5-orders of magnitude. This behaviour agrees with published kernels of this imager under similar simulation conditions [12]. At distance less than 1.0 cm from the center, the rate of decrease is found to be most rapid. Beyond 1.0 cm, the response starts to level off and settles down to the range between 10^{-7} and 10^{-8}.

4.3.1. 6MV X-ray Beam Energy Spectrum

The 6MV photon beam for Clinac 2100 EX was simulated with BEAMnrc. The energy spectrum of the results was calculated (Figure 3-3). A peak is observed at the 511 keV bin which can be attributed to the small amount of annihilation of positrons from the process of pair production. In comparison to Mohan's kernel, the 2100EX kernel generated in this study shows a higher spectral resolution and a higher weighting in low energy. Mohan's kernel also does not capture the annihilation of positron. Because of the higher binning, 2100 EX spectrum is a more realistic spectrum. The average energy for the 2100 EX and Mohan's spectrum are 1.08 MeV and 1.12 MeV respectively

4.3.2. Scatter Kernel Simulation

Using the energy spectrum obtained in the previous section, the scatter kernel of the flat panel EPID was calculated in DOSRZnrc. Figure 3-4 shows the calculated flat panel EPID scatter

kernel which is normalized to the central axis of beam. The x-axis depicts the distance in centimeters from the central axis of the photon beam.

4.4. Verification

4.4.1. Verification of Monte Carlo Simulation

4.4.1.1. Spectral Effect

The kernels from both spectra fall within the same order of magnitude (Figure 3-5). At a distance of less than 0.3 cm from the center, the relative scatter factor increases to a value of +0.15 (Figure 3-6). Beyond 0.3 cm, the relative scatter factor decreases rapidly to -0.2. This implies that the 2100EX spectrum has more relative scatter than Mohan's spectrum. The relative scatter factor remains at this level as the distance from the center of the field increases. This can be attributed to the differences in the shape and average energy between the two spectra. As photons with higher energy have higher probability to be scattered in the forward direction in Compton scattering, kernels with higher proportion of high energy photons will exhibit less lateral scattering. Mohan's spectrum has a higher proportion of high energy photon with an average energy of 1.12 MeV (see Figure 3-3) than the 2100EX spectum with an average energy of 1.08 MeV. As a result, it exhibits less lateral scattering relative to the 2100EX in the region far away from the center and has relatively more interaction in the region closer to the center of the incident beam.

Comparing the 15MV photon beam kernels, both 6MV and 15MV kernels (Figure 3-7) are significantly different with the 6MV kernel decreasing significantly faster. The results show that the 6MV kernel exhibits more relative scatter at distance greater than 0.5 cm from the center than the 15MV case. In the region less than 0.5 cm away, the relative scatter factor increases rapidly to +0.3 (Figure 3-8). Beyond the point of 0.5 cm, the relative scatter factor decreases rapidly to about -0.5 and remains at this level. As 15MV has a higher average energy than 6MV beam, it is expected that the relative scatter factor will exhibit similar behaviour as in the previous section. The higher magnitude swing from +0.35 to -0.50 than in the previous case can be attributed to the higher average energy difference between the two beams.

4.4.1.2. Phantom Effect

Compared to the scatter kernel generated at d_{max} in a water phantom, the profile of the kernels of the two phantoms are significantly different (Figure 3-9). The flat panel imager kernel exhibits more scatter in the region outside of 1.0 cm away from the center (Figure 3-10). In this region, the relative scatter factor decreases to -0.8. At less than 1.0 cm, the flat panel scatter kernel has less scatter than the water case with the maximum relative scatter value of +2.8. This implies that the scatter kernel behaviour of the flat panel imager is very different from that of water and cannot be approximated as a water phantom. For the two-dimensional dosimetry application, a

two dimensional calibration is required to calibrate each pixel on the imager to the appropriate water equivalent dose.

Comparing the two effects, it is evident that phantom effect is the most significant in this study.

4.4.2. Experimental Verification

4.4.2.1. Deconvolution Kernel

This check is important because the deconvolution operation is prone to noise corruption and can result in an inoperable function. The form of the deconvolution kernel is a high pass filter which can be confirmed by observing the shape of the resulting 2D plot (Figure 3-11)

4.4.2.2. Test Pattern

By inspecting the two images, the quality of images captured by both devices are comparable and of high quality (Figure 3-12). However, for dosimetry applications, it is necessary to calibrate acquired data from both film and the flat panel imager to obtain the dose information.

4.4.2.3. Profile Comparison

To assess the effectiveness of the deconvolution method, the acquired 2-D dose distribution in both flat panel imager and film are compared. The profiles in this section are normalized at the center of the test pattern. The relative dose profiles along both the radial and transverse directions (Figure 3-13) from film and flat panel EPID are plotted without applying the deconvolution method. Along the x direction, the imager data show over response at the low dose region in-between peaks as well as outside the main field area. Along the y direction, the imager shows overall over response compared to the film. Figure 3-14 shows the profiles captured from film (red) and the flat panel imager (blue) along the center of the image with the deconvolution correction. About 5% improvement in the agreement between the two profiles is observed around the low dose region inside the field. In the high dose region, the discrepancy between the EPID and the film is improved but still exceeds 3%. This is attributed to the over response within the detector caused by radiation damage of the electronics from normal wear and tear. Although this may not affect the quality of imaging, it has a significant impact on the dosimetry and should be addressed before this technique is implemented clinically. The investigation of this issue is beyond the scope of this study and warrants further investigation. Two peaks are also observed in the film profiles outside the radiation field which are attributed to the registration marks on the film.

5. Conclusions

The results presented demonstrate that the Varian amorphous silicon flat panel portal imager may be calibrated as a water equivalent 2D dosimeter for use in IMRT dose verification. We measured an inherent build-up of 1.1 cm of water- equivalent material, which enables this detector to generate clinically acceptable two-dimensional dose distributions without any additional build-up material. We also found that the EPID has a linear response with dose. From the calculation verification studies, we determined that the dosimetric property of the imager was significantly different from that of water. We found that higher energy beams (both in terms of maximum energy and average energy) provided less scatter than lower energy beams. Due to the higher atomic number, the flat panel EPID was found to have significantly more scattering power than water. By measuring variation of scatter with radiation spectrum and phantom material, the phantom material was determined to have the higher scattering effect. We demonstrated that the non-water equivalent property of the flat panel EPID may be corrected using the deconvolution method. This result shows that the amorphous silicon imager has the ability to act as a dosimeter with a high degree of relative dose accuracy. It also demonstrates considerable potential in the application of IMRT verification.

6. References

[1] Ling, C. et. al., “A Practical Guide to Intensity-Modulated Radiation Therapy”, Medical Physics, Madison, 2003.

[2] Ezzell, G. et. al., “Guidance document on delivery, treatment planning, and clinical implementation of IMRT: Report of IMRT subcommittee of the AAPM radiation therapy committee”, Med. Phys., 30 (8), August 2003.

[3] Partridge, M. et al, “IMRT verification by three-dimensional dose reconstruction from portal beam measurements”, Med. Phys., 29(8), August 2002

[4] Essers, M. et al., “In vivo dosimetry during external photo beam radiotherapy”, Int. J. Radiat. Oncol., Biol., Phys. 43, 245- 256 (1999)

[5] Bortfeld, T. et al., “Realization and verification of three-dimensional conformal radiotherapy with modulated fields”, Int. J. Radiat. Oncl., Biol., Phys. 30, 899-908 (1994).

[6] Boyer A.L. et. al, “A review of electronic portal imaging devices”, Medical Physics: 19(1), Jan, 1992.

[7] Van Dyk, J. et al, “The Modern Technology of Radiation Oncology”, Medical Physics, Chp. 13

[8] Antonuk, L.E., “Electronic portal imaging devices” a review and historical perspective of contemporary technologies and research”, Physics in Medicine and Biology: 47 (2002)

[9] Muro, P. et al., “X-ray quantum limited portal imaging using amorphous silicon flat-panel arrays”, Med. Phys., 25(5), May 1998

[10] McCurdy, B. M. et al., “Dosimetric investigation and portal dose image prediction using an amorphous silicon electronic portal imaging device”, Med. Phys. 28(6), 911-924 (2001).

[11] Wang, X. et al, “Dosimetric Verification of intensity-modulated fields”, Med. Phys. 23, 317-327 (1996)

[12] Warkentin, B., et al., “Dosimetric IMRT verification with a flat-panel EPID”, Med. Phys 30, 3143 – 3155 (2003).

[13] Chang, J. et al., “An iterative EPID calibration procedure for dosimetric verification that considers the EPID scattering factor”, Med. Phys. 28(11), 2247-2257 (2001).

[14] Chang, J. et al., “Relative Profile and dose verification of intensity-modulated radiation therapy,” Int. J. Rad. Onc. Biol. Phys. 47(1), 231-240 (2000).

[15] Heijman, B.J.M. et al., “Portal dose measurement in radiotherapy using an electronic portal imaging device (EPID),” Phys. Med. Biol., 40, 1943-1955 (1995).

[16] K.L. Pasma, “Dosimetry with a Fluoroscopic Electronic Portal Imaging Device,” Ph.D. thesis, Erasmus University Rotterdam, The Netherlands, September 1999.

[17] Keller, H. et al., “Calibration of a portal imaging device for high-precision dosimetry: A Monte Carlo study,” Med. Phys. 23, 1601-1611 (1998).

[18] Pasma, K.L. et al., “Accurate portal dose measurement with a fluoroscopic electronic portal imaging deice for open and wedged beams and dynamic multileaf collimation,” Phys. Med. Biol. 43(8), 2047-2060 (1998).

[19] El-Mohri, Y. et al., “Relative Dosimetry using active matrix flat-panel imager (AMPFI) technology”, Med. Phys. 26(8), 1530-1541, 1999.

[20] Grein, E. et al., “An investigation of a new amorphous silicon electronic portal imaging device for transit dosimetry”, Med. Phys. 29(10), 2262-2267, 2002.

[21] Johns, H. et. al., “The Physics of Radiology”, Chales C Thomas, Springfield, 1983.

[22] Kawrakow, I. et al. “The EGSnrc Code System: Monte Carlo simulation of electron and photon transport”, Technical Report PIRS-701, National Research Council of Canada, Ottawa, Canada, 2000.

[23] D. W. O. Rogers et. al., “BEAM: A Monte Carlo code to simulate radiotherapy treatment units”, Med. Phys., 22:503 - 524, 1995.

[24] Treurniet, J. et. al., “BEAMnrc, DOSXYZnrc and BEAMDP GUI User's Manual”, NRC Report PIRS 0623(rev C), 2004.

[25] Kawrakow, I., “Accurate condensed history Monte Carlo simulation of electron transport. I. EGSnrc, the new EGS4 version”, Med. Phys., 27:485 - 498, 2000.

[26] Karmark, C.J. et al, “A primer on theory and operation of linear accelerators in radiation therapy”, Medical Physics Publishing, Madison, 1996

[27] Mohan, R. et. al., “Energy and angular distribution of photons from medical linear accelerators”, Med. Phys., 12 (5), Sep. 1985.

[28] Mohan R. et al., “Use of fast Fourier transforms in calculating dose distributions for irregularly shaped fields for three-dimensional treatment planning”, Med. Phys. 14(1), 70-77 (1987).

[29] McNutt, T.R. et al., “Calculation of portal dose using the convolution/superposition method,” Med. Phys. 23(4), 1996.

[30] Munro, P., “Portal imaging technology: Past, present, and future”, Semin. Radiat. Oncol. 5 115 – 133 (1995).

[31] Partridge, M. et al., “Optical scattering in camera-based electronic portal imaging”, Phys. Med. Biol. 44, 2381-2396, 1999.

[32] Chang, J. et al., “Using the frame averaging of aS500 EPID for IMRT verification”, J. of Appl. Clin. Med. Phys., 4(4), 287-299 (2003).

[33] Zhu, Y. et al., “Portal dosimetry using a liquid ion chamber matrix: Dose response studies,” Med. Phys. 22(7), 1101 – 1106 (1995).

[34] Siewerdsen, J.H. et al., “Empirical and theoretical investigation of the noise performance of indirect detection, active matrix flat-panel imagers (AMFPIs) for diagnostic radiology”, Med. Phys., 24(1), 71-89, 1997.

[35] McCurdy, B.M.C. et al., “A two-step algorithm for predicting portal dose images in arbitrary detectors”, Med. Phys. 27, 2109-2116 (2000).

[36] Portal Vision 6 user manual, Varian.

Appendix I. SLIC and Video-Based EPIDs

I.A. Scanning Liquid Ionization Chamber (SLIC)

This system was developed at Nederlands Kanker Institueet (NKI). It is based on the latent image resulting from the ion generated inside the liquid during the radiation [1][6] and is usually referred to as liquid film. Typically, 2,2,4-trimethylpentane is used as the medium. It uses a 1.0-mm-thick stainless steel front screen acting as the main radiation build-up material to which a bank of (typicall of a size of 256x256) ionization chambers is adhered (Figure I-1). The chambers are constructed by using a set of 256 strip-formed electrodes with another set of 256 high voltage electrodes overlayed on top and submerged together in the liquid film. These two sets are connected and positioned perpendicularly forming a mesh like structure. The crossed points of the two sets form a matrix of small ion chambers. Each high voltage strip and lower electrode is connected to a high voltage switch and high sensitive electrometer. When radiation enters the liquid film, ionization will occur generating secondary electrons which forms a latent image that lasts for 0.3s. Further irradiation or increase in read voltage will not improve the signal size or quality. High voltage (typically at around 300V) is applied periodically to each top strip at an interval of 20ms to activate a whole row of chambers and the values in these chambers (usually two to three at a time) are read via the electrometers. To acquire a whole image, it takes from 1.3s to 5.9s depending on the image quality and noise level [6]. With the memory characteristics of the liquid film, the image quality is better than expected. However, the time required to acquire a whole image is considered too long for intensity modulation radiation therapy. The size of the matrix is also limited to 256x256 which does not provide high enough spatial resolution. Its quantum utilization also falls short of an ideal detector [7].

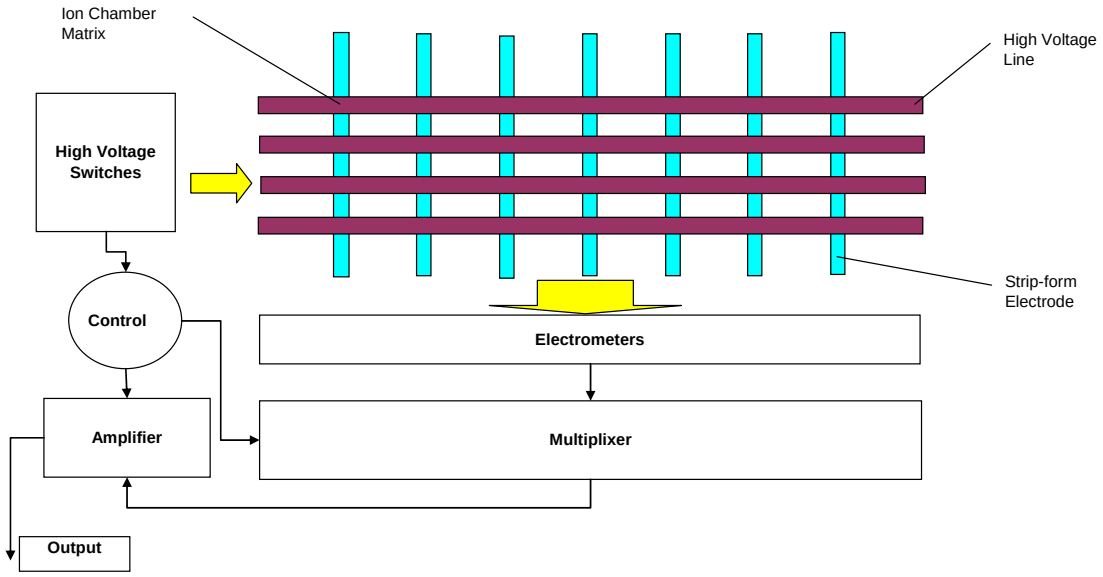

Figure I-1 This shows a schematic of a SLIC EPID. High voltage switches turn on the high voltage lines one at a time to turn on the horizontal array of ion chambers. The readings are read out via the electrometers which are multiplexed and sent to output via an amplifier.

I.B. Video-Based EPID

The Video-based EPID uses a metal/phosphor screen placed perpendicular to the beam as a build-up layer and a scintillation screen to generate visible light from the incident photon. It is therefore considered to be an indirect detector. A mirror is placed directly beneath the screen inclined at a 45° angle to direct the received light to a video camera for recording. Figure I-2 shows a typical set-up of a video-based EPID system. The obvious advantage of this system is its ability to monitor the localization in real-time. Typically, it has the largest coverage area relative to other EPIDS implying that all radiation exiting the patient has the opportunity to generate images. On the downside, however, this design suffers from low quantum efficiency due to light loss at the mirror and lens. Only 0.1% to 0.01% of light generated from phosphor screen reaches the camera [6][7]. The large aperture lenses that are usually employed in this system tend to show significant distortion, vignetting, and low depth of view. By having a fixed angle mirror, it assumes exit light travels in one direction.

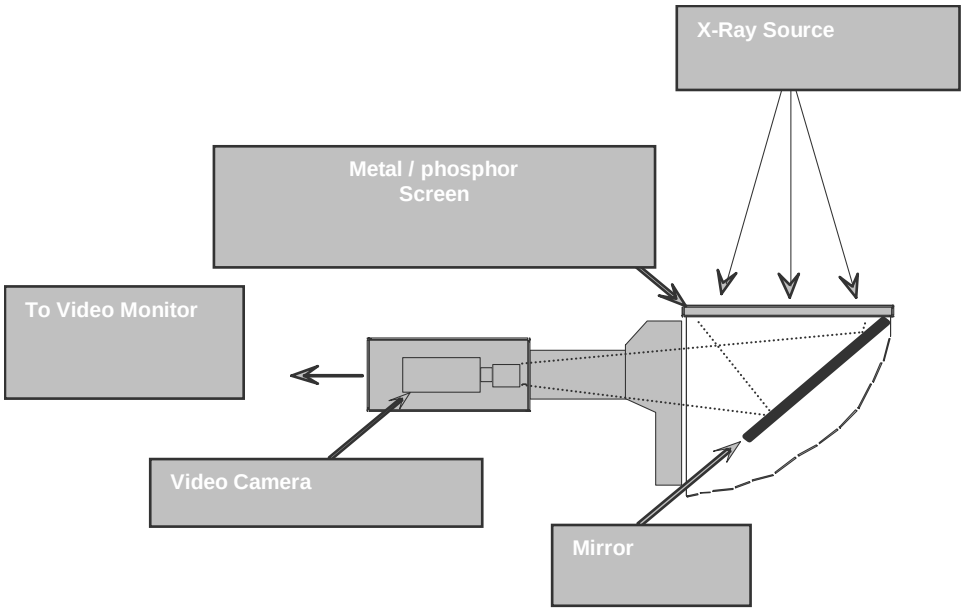

Figure I-2: Video-based EPID consists of a video camera store connected to a video monitor outside the treatment room. A metal/phosphor screen is used for converting x-ray to visible light which is directed to the camera via a mirror.

Appendix II. Other Dose Calculation Methods

The two dimensional photon fluence, ϕ, of an incident photon beam irradiating any phantom or detector is assumed to be the sum of the superposition of individual pencil beams. The deposited 2D dose distribution, D, is assumed to be the result of the convolution of the incident photon fluence and the scatter kernel, k, of the phantom or detector. This method has been shown to give a good dose prediction in phantom [28][29]. The 2D dose distribution can be expressed as:

$$D = k \otimes \phi \qquad \text{(II-1)}$$

where

D(x,y)	=	two dimensional dose distribution;
k(x,y)	=	two dimensional dose scatter kernel; and
ϕ(x,y)	=	photon fluence.

From the above equation, changes in the scatter kernel, k, will give the different dose distribution with unchanged incident photon fluence condition. In other word, the dose distribution of a material with a scatter kernel, k, can be derived by knowing the incident photon fluence. In radiation dosimetry, the primary goal is to determine the dose deposition in water. But measurement devices, like in this case flat panel imager, are not water equivalent. This is important in calibrating the flat panel imager to water. To determine the equivalent dose in water, the 2D measured data from the imager have to be converted using the scatter kernel information. The accuracy of the kernel has a direct implication on the resulting accuracy of the calibrated dose and it is important that the kernel is accurately modeled.

The scatter kernel is decomposed into the high energy and low energy scatter components. High energy scatter, k_s, is defined as the scattering from the high energy x-ray interactions with the components of the detector. Low energy scatter, k_g, is defined the scatter from the low energy photon scatter (mainly in the visible photon range) at the scintillation layer which is sometimes referred as glare. For accurate modeling, this phenomena is incorporated as it directly affects the dosimetric behaviour of the scintillator based devices [12][10][15][30][31]. By convolving the two kernels, the dose scatter kernel can be obtained as shown below:

$$k = k_s \otimes k_g \qquad \text{(II-2)}$$

II.A. Empirical Method

Chang et al. initially developed an empirical calibration method for SLIC EPID and later adapted it for a flat panel EPID. It uses convolution[32], TMR, and an EPID phantom scatter factor (S_{pe})[33] based on pencil beam convolution[28], assuming the flat panel to be a non-water equivalent phantom with the EPID phantom scatter factor S_{pe}. This factor is defined as the ratio of field size

corrected dose measurement at two different field sizes. The measurements are made at a small region at the center of the detector set at constant source to detector distance (SDD) [33]:

$$S_{pe}(r') = \frac{M_{EPID}(r')}{M_{EPID}(r_o')} \frac{S_c(r_o)}{S_c(r)} \qquad \text{(II-3)}$$

where

r	=	field size defined at SAD;
SAD	=	source to isocenter distance;
r'	=	r x SSD/SAD;
SSD	=	source to surface distance;
r_o	=	10x10 cm at SAD;
M_{EPID}	=	average pixel value of a small region at the central axis of the EPID; and
$S_c(r)$	=	collimator factor at field size r.

The measured profile at SSD is transformed to SAD in air by back-projection, inverse square correction, and phantom scatter factor correction. Figure II-1 shows a schematic of the operation.

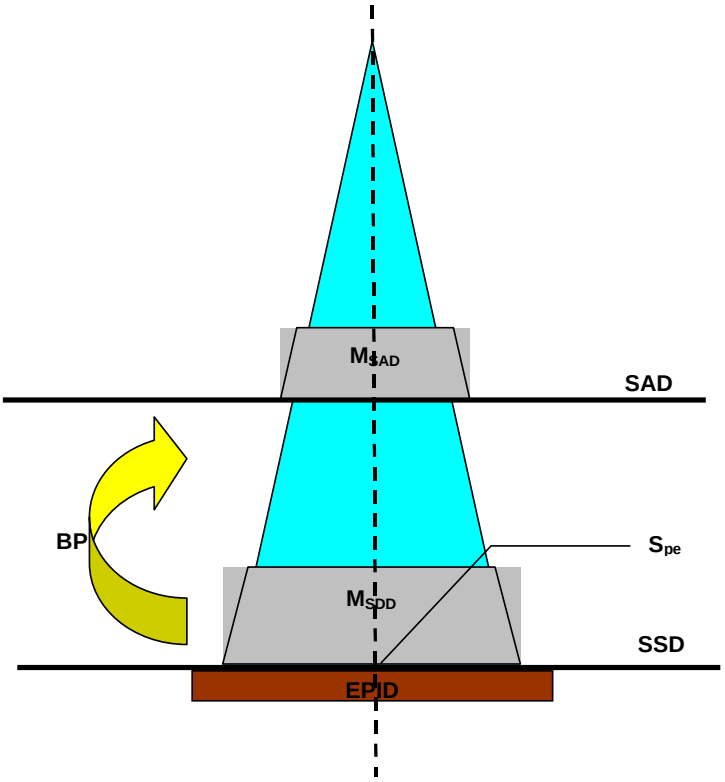

Figure II-1 flat panel imager, EPID, measures a profile at Source to Detector Distance (SDD), M_{SDD}, which is back-projected to SAD to become M_{SAD}.

$$M_{SAD} = BP(M_{SSD})\left[\frac{SSD}{SAD}\right]^2 \frac{1}{S_{pe}(r_{p,SDD})} \qquad \text{(II-4)}$$

where

BP	=	Back-projection operator; and
$r_{p,SDD}$	=	equivalent square field size at SDD.

The scatter contribution to the profile is assumed to be merely a percentage of total response instead of a convolution relation. The 2D dose distribution in a water equivalent material is determined by convolving the in air profile M_{SAD} with a standard depth scatter kernel at a 10x10 cm^2 field size. For a profile at any arbitrary field size $r_{p,SAD}$, TMR ratios are used for correction. The relationship is given below.

$$D_d = M_{SAD} \otimes h_s\left[\frac{TMR(d, r_{p,SAD})}{TMR(d, 10x10)}\right] \qquad \text{(II-5)}$$

where

D_d	=	dose distribution at depth d;
M_{SAD}	=	measured profile at SAD;
h_s	=	depth scatter kernel of tissue equivalent kernel at the depth d; and a field size of 10x10 cm^2;
$r_{p,SAD}$	=	equivalent square field size at SAD.

This approach uses one scatter phantom factor to calibrate the EPID. However, the scatter phantom factor is field size dependent. In the case of IMRT, this is insufficient as no clear field size can be defined. The tissue equivalent scatter kernel does not incorporate glare effect. This method is not appropriate for IMRT verification [12].

II.B. Two-Step Convolution Algorithm

Siewerdsen et al. [34] first proposed that a flat panel EPID may be represented by a linear time-invariant cascade system. Each component of the device may be modeled as a linear system with a transfer function of $H_k(s)$. In a cascade linear system, the system transfer function is determined as a product of the transfer function of each layer.

$$H(s) = \prod_k H_k(s) \qquad \text{(II-6)}$$

The transfer function describes the response of the corresponding layer or component given an input signal and is dictated by the physical behaviour of the layer of interests. McCurdy et al.

[10] used Monte Carlo simulation and an empirical method to model a flat panel EPID. Instead of modeling the transfer function of each component, the system transfer function was decomposed into two components, scattered fluence kernel (k_s) and glare kernel (k_g) in spatial domain.

$$k = k_s \otimes k_g \qquad \text{(II-7)}$$

The Monte Carlo simulation was used to derive the scatter kernel. Although the computational time for the kernel is long, this calculation only is evaluated once.

The glare kernel here was determined by Heijmen et al [15] for a video-based EPID. Later, McCurdy[35] used a double exponential function to fit the tail. A delta function was then used to empirically adjust the function to fit the calculated profile to the measurement. The function is represented as:

$$k_g = \delta + \alpha(e^{-ar} + \beta e^{-br}) \qquad \text{(II-8)}$$

where δ = delta function;

α, β, a, b = empirical values; and

r = spatial distance from the centre of the function to any point of interest.

Using these kernels, the dose distribution may be predicted on the detector plane given the input photon fluence, ϕ.

$$D_p = (k_s \otimes k_g) \otimes \phi \qquad \text{(II-9)}$$

where

$D_p(x,y)$ = predicted two dimensional dose distribution;

$\phi(x,y)$ = incident photon fluence onto the detector.

The incident photon fluence above involves a separate calculation using geometric ray tracing[35] or direct measurement on the field of interest. By convolving the photon fluence, the predicted dose can be determined for calibration.

The results presented by McCurdy indicate a good match between the predicted dose and measurement by the EPID. Unlike the empirical method, scatter onto each pixel was properly accounted for using convolution. Glare was also taken into consideration using a generic glare kernel. The energy spectrum used was based on an interpolation spectrum and not specifically designed for the LINEAR ACCELEARTOR used. The glare kernel used was designed for video-based EPID. These factors could affect the accuracy of the results. The incident fluence was measured using a scanning ion chamber. This measurement has to be made for every field of interest which can be time consuming. McCurdy also suggested that a generic ray tracing or a fluence map generated from a treatment planning system could be used. However, no literature on the accuracy of this method on a flat panel EPID has been reported. The goal of this method

is to predict the dose deposited on the portal imager but no provision was made to predict the dose deposition in the target volume.

Appendix III. Matlab Codes for Registration

III.A. Top Level Program

```
% This is a top level test bench for the portal imager
% written by:   Gary Lim
% Version:      3.0
% Date:         Sept 13, 2003

clc;
clear;

set(gcf, 'Renderer', 'zbuffer');

%load up the dicom step wedge file
[portal.calfname, portal.calpname] = uigetfile('*.dcm', '');
portal.caldata = mydicomread(portal.calfname);
portal.info = dicominfo(portal.calfname);

%load up the efl step wedge file
[cadplan.calfname, cadplan.calpname] = uigetfile('*.efl', '');
[cadplan.info, cadplan.caldata] = eflread(cadplan.calfname);


pic_dcm = 1;
pic_efl = 2;
figure(pic_dcm);
montage(portal.caldata,[]);
figure(pic_efl);
montage(cadplan.caldata,[]);
zoom(2);

%reference point acquisition
%hit "Return" to finish acquisition
regpoint_dcm = PointCapture(pic_dcm);
regpoint_efl = PointCapture(pic_efl);
pause(2);

%Calculate the centroid displacement and fiducial covariance matrix H
[centdisp_efl, centdisp_dcm, H] = SWCentroid(regpoint_efl, regpoint_dcm);
[R, S, T] = regMatrix(H, centdisp_efl, centdisp_dcm, regpoint_efl, regpoint_dcm);
size_dcm = size(portal.caldata);
new_data_efl = srt_efl1(S,R,T,size_dcm,cadplan.caldata);
%new_data_efl = dcoffset(new_data_efl);
cadplan.caldata = new_data_efl;
figure(3);
montage(new_data_efl, []);

totalframe = input('Please enter the total number frames: ');
doserate = input('Please enter the dose rate used: ');
dcmtemp = portal.caldata;
portal.caldata = doserate*totalframe*dcmtemp;
[cal_out, p] = stpwdg_cal(cadplan.caldata, portal.caldata, 3);
cal_plot(cal_out, 4);
```

```
pause(1);
%[pic_diff, dcm_result, efl_result] = diffcal(cadplan.caldata, portal.caldata, cal_out);
[pic_diff, dcm_result, efl_result, normal_pt, ndcm] = diffcal2(cadplan.caldata, portal.caldata,
cal_out);
[row_s, col_s] = size(dcm_result);
diffplot(pic_diff, 7);
cent_plot(dcm_result, efl_result, 7, 8);
```

III.B. Program: mydicomread.m

```
function [OutputData, OutputMap] = mydicomread(filename)
%This takes a dicom file and covert it into matlab file
%it also uses the minimum value to convert the image starting from 0
[rawData,In_map] = dicomread(filename);
%Converting 16 bits unsigned integer to double precision
rawData = double(rawData) + 1;
%dc_offset = 32765;  %Emperical data
%OutputData = -(rawData - dc_offset);
OutputData = -rawData;
OutputMap = [];
%16 bit conversion
%OutputData = im2bit(OutputData, 16);
```

III.C. Program: eflread.m

```
function [header, FluenceOutput] = eflread(filename)
%This file was written by Gary Lim
%Version:  1.0
%Date:  February 27, 2003
%Purpose:  This function reads in EFL file and convert into header and data
[fid,message] = fopen(filename,'rt');
header = 'This is the header';
headerFlag = 0;
while headerFlag == 0
   CurrentLine = fgetl(fid);
   header = strvcat(header,CurrentLine);
   [rowValue, ColumnValue] = size(header);
   CurrentHeader = header(rowValue,:);
   if CurrentHeader(1:12) == 'NumberOfRays'
      headerFlag = 1;
   else
      CurrentHeader4 = CurrentHeader(1:4);
      switch CurrentHeader4
         case 'NumX'
            x_width = str2num(CurrentHeader(6:length(CurrentHeader)));
         case 'DimX'
            scale = str2num(CurrentHeader(6:length(CurrentHeader)));
         case 'NumY'
            y_width = str2num(CurrentHeader(6:length(CurrentHeader)));
         otherwise
            headerFlag = 0;
      end
   end
end
FluenceData = fscanf(fid,'%5d %g', [2,inf]);
fclose(fid);
```

```
FluenceData = FluenceData';
FluenceRaw = zeros(y_width, x_width);
rsize = 256;
csize = 256;
FluenceOutput = zeros(rsize, csize);  %useful size
rlowerbound = round((y_width-rsize)/2);
clowerbound = round((x_width-csize)/2);
for FluenceCounter = 1:length(FluenceData)
   currentcounter = FluenceData(FluenceCounter, 1);
   FluenceRaw(currentcounter) = FluenceData(FluenceCounter,2);
end
for rcounter = 1:rsize
   raw_row = round(rcounter + rlowerbound);
   for ccounter = 1:csize
      raw_col = round(ccounter + clowerbound);
      FluenceOutput(rcounter, ccounter) = FluenceRaw(raw_row, raw_col);
   end
end
scale = 4;
FluenceOutput = imresize(FluenceOutput, scale, 'bilinear');
FluenceOutput = imrotate(FluenceOutput, 90);
```

III.D. Program: pointcapture.m

```
function Pointxy = PointCapture(FigureHandle)
%Written By:    Gary Lim
%Date:          March 4, 2003
%Version:       1.0
%Description:   This function takes in the figure handle and
%               obtain the x and y coordinates of the unlimited points
%               in the figure.  Press 'Enter' to finish.

figure(FigureHandle);
[x_coor, y_coor] = ginput;
hold on;
plot(x_coor, y_coor, 'r+');
hold off;
Pointxy = [x_coor,y_coor];
```

III.E. Program: swcentroid.m

```
function [output_efl, output_dcm, fid_cov] = SWCentroid(data_efl, data_dcm)
%calculate the mean value
%Written by      Gary Lim
%Version:        1.0
%This subroutine is designed to calculate centroid for registration
avg_efl = mean(data_efl);
avg_dcm = mean(data_dcm);
output_efl = Centroid_disp(data_efl, avg_efl);
output_dcm = Centroid_disp(data_dcm, avg_dcm);
fid_cov = cov(data_efl, data_dcm);
```

III.F. Program: regMatrix.m

```
function [R, S, T] = regMatrix(H, centdisp_efl, centdisp_dcm, regpoint_efl, regpoint_dcm)
%This function is used to calculate the rotation matrix R, scaling matrix
```

```
%S in registration of the step wedge between
%fluence file (efl) and as500 (dcm) files.
%Input:     H              - fiducial matrix
%           centdisp_efl   - centroid displacement of efl file
%           centdisp_dcm   - centroid displacement of dcm file
%written by:    Gary Lim
%version:       1.0
%date:          May 13, 2003

[U,Lamda, V] = svd(H);
% Calculation the Rotational Matrix
R = V*diag([1 det(V*U)])*U';
% Calculation of the scaling factor
S_numerator = 0;
S_denominator = 0;
for S_counter = 1:length(centdisp_efl)
   S_numerator = S_numerator + (R*centdisp_efl(S_counter,:)')'*centdisp_dcm(S_counter,:)';
   S_denominator = S_denominator + centdisp_efl(S_counter,:)*centdisp_efl(S_counter,:)';
end
S = S_numerator/S_denominator;
% Calculation of the translational vector
T = mean(regpoint_dcm)'-S*R*mean(regpoint_efl)';
```

III.G. Program: srt_efl1.m

```
function Output_Matrix = srt_efl1(S, R, T, size_dcm, data_efl)
%This function transform the raw efl file to dcm file with size size_dcm
%(m x n)
%Written by:    Gary Lim
%Version:       1.0
%Date:          May 27, 2003

Output_Matrix = zeros(size_dcm);
min_mask = min(min(data_efl));
size_efl = size(data_efl);
for y_counter= 1:size_dcm(1)
   for x_counter = 1:size_dcm(2)
      coor_efl = (S^-1)*inv(R)*([x_counter y_counter]' - T);
      xc = coor_efl(1);
      yc = coor_efl(2);
      xd = floor(xc);
      xu = ceil(xc);
      yd = floor(yc);
      yu = ceil(yc);
      coor_type = checktype(coor_efl, size_efl);
      switch(coor_type)
         case 0
            point00 = data_efl(yd, xd);
            point01 = data_efl(yd, xu);
            point10 = data_efl(yu, xd);
            point11 = data_efl(yu, xu);
            mag_upper = point00 + (xc-xd)/(xu-xd)*(point01-point00);
            mag_lower = point10 + (xc-xd)/(xu-xd)*(point11-point10);
            mag = mag_upper + (yc-yd)/(yu-yd)*(mag_lower-mag_upper);
         case 1
            point10 = data_efl(yu, xd);
```

```
            point11 = data_efl(yu, xu);
            mag = point10 + (xc-xd)/(xu-xd)*(point11-point10);
        case 2
            point01 = data_efl(yd, xu);
            point11 = data_efl(yu, xu);
            mag = point01 + (yc-yd)/(yu-yd)*(point11-point01);
        case 3
            mag = data_efl(round(yc), round(xc));
        case 4
            point00 = data_efl(yd, xd);
            point01 = data_efl(yd, xu);
            mag = point00 + (xc-xd)/(xu-xd)*(point01-point00);
        case 6
            mag = data_efl(round(yc), round(xc));
        case 8
            point00 = data_efl(yd, xd);
            point10 = data_efl(yu, xd);
            mag = point00 + (yc-yd)/(yu-yd)*(point10-mag_upper);
        case 12
            mag = data_efl(round(yc), round(xc));
        otherwise
            %warning('it is out of bound');
            mag = min_mask;
    end
    Output_Matrix(y_counter, x_counter) = mag;
  end
end
```

Appendix IV. Monte Carlo Simulation Input File

```
TITLE= EPID_aS500_SSD138_6MV

###########################
:start I/O control:

IWATCH= off
STORE INITIAL RANDOM NUMBERS= no
IRESTART= first
STORE DATA ARRAYS= yes
OUTPUT OPTIONS= dose summary
ELECTRON TRANSPORT= normal
DOSE ZBOUND MIN= 1
DOSE ZBOUND MAX= 61
DOSE RBOUND MIN= 0
DOSE RBOUND MAX= 60

:stop I/O control:
###########################

###########################
:start Monte Carlo inputs:

NUMBER OF HISTORIES= 100000000
INITIAL RANDOM NO. SEEDS= 705, 1028
MAX CPU HOURS ALLOWED= 90.000
IFULL= dose and stoppers
STATISTICAL ACCURACY SOUGHT= 0.0000
SCORE KERMA= no

:stop Monte Carlo inputs:
###########################

###########################
:start geometrical inputs:

METHOD OF INPUT= groups
Z OF FRONT FACE= 0.
NSLAB= 3, 8, 4, 2, 2, 5
SLAB THICKNESS= 10, 1, 0.1, 0.017, 0.055, 0.5
RADII= 0.01, 0.0695, 0.1, 0.2, 0.4, 0.6, 0.8, 1, 1.5, 2, 2.5, 3, 3.5, 4, 4.5, 5, 6, 7, 8, 9, 10, 12.5, 15
MEDIA= AIR521ICRU,
 CU521ICRU,
 EPID_Scin,
 PYREX521ICRU,
 H2O521ICRU;

DESCRIPTION BY= planes
MEDNUM= 1, 2, 3, 4, 5
START ZSLAB= 1, 15, 16, 18, 20
STOP ZSLAB= 14, 15, 17, 19, 24
START RING= 1, 1, 1, 1, 1
STOP RING= 23, 23, 23, 23, 23
```

```
:stop geometrical inputs:
##########################

###########################
:start source inputs:

INCIDENT PARTICLE= photon
SOURCE NUMBER= 0
SOURCE OPTIONS= 0.069, 0, 0, 1
INCIDENT ENERGY= spectrum
SPEC FILENAME= C:\egsnrc\EGS_HOME\6MVspectrum.spectrum
SPEC IOUTSP= include

:stop source inputs:
##########################

###########################
:start MC transport parameter:

Global ECUT= 0.521
Global PCUT= 0.001
Global SMAX= 1e10
ESTEPE= 0.25
XImax= 0.5
Skin depth for BCA= 3
Boundary crossing algorithm= EXACT
Electron-step algorithm= PRESTA-II
Spin effects= on
Brems angular sampling= KM
Brems cross sections= BH
Bound Compton scattering= Off
Pair angular sampling= Simple
Photoelectron angular sampling= Off
Rayleigh scattering= Off
Atomic relaxations= On
Set PCUT= 0
Set PCUT start region= 1
Set PCUT stop region= 1
Set ECUT= 0
Set ECUT start region= 1
Set ECUT stop region= 1
Set SMAX= 0
Set SMAX start region= 1
Set SMAX stop region= 1

:stop MC transport parameter:
##########################

###########################
:start variance reduction:

BREM SPLITTING= off
NUMBER OF BREMS PER EVENT= 1
CHARGED PARTICLE RUSSIAN ROULETTE= off
ELECTRON RANGE REJECTION= off
ESAVEIN= 0.0
```

```
RUSSIAN ROULETTE DEPTH= 0.0000
RUSSIAN ROULETTE FRACTION= 0.0000
EXPONENTIAL TRANSFORM C= 0.0000
PHOTON FORCING= off
START FORCING= 1
STOP FORCING AFTER= 1
CS ENHANCEMENT FACTOR= 1
CS ENHANCEMENT START REGION= 1, 1
CS ENHANCEMENT STOP REGION= 1, 1

:stop variance reduction:
##########################

###########################
:start plot control:

PLOTTING= on
LINE PRINTER OUTPUT= off
EXTERNAL PLOTTER OUTPUT= on
EXTERNAL PLOT TYPE= Both
PLOT RADIAL REGION IX= 1, 2, 3, 4, 5, 6, 7, 8, 9, 10
PLOT PLANAR REGION IZ= 10, 11, 12, 13, 14, 15, 16, 17, 18, 19, 20, 21, 22, 23, 24

:stop plot control:
##########################
```